

Retrievals of riming and snow density from vertically-pointing Doppler radars

Article

Accepted Version

Mason, S. L. ORCID: <https://orcid.org/0000-0002-9699-8850>,
Chiu, C. J., Hogan, R. J., Moisseev, D. and Kneifel, S. (2018)
Retrievals of riming and snow density from vertically-pointing
Doppler radars. *Journal of Geophysical Research:*
Atmospheres, 123 (24). pp. 13807-13834. ISSN 2169-8996
doi: <https://doi.org/10.1029/2018JD028603> Available at
<https://centaur.reading.ac.uk/80877/>

It is advisable to refer to the publisher's version if you intend to cite from the work. See [Guidance on citing](#).

To link to this article DOI: <http://dx.doi.org/10.1029/2018JD028603>

Publisher: American Geophysical Union

All outputs in CentAUR are protected by Intellectual Property Rights law, including copyright law. Copyright and IPR is retained by the creators or other copyright holders. Terms and conditions for use of this material are defined in the [End User Agreement](#).

www.reading.ac.uk/centaur

CentAUR

Central Archive at the University of Reading

Reading's research outputs online

Retrievals of riming and snow density from vertically-pointing Doppler radars

S. L. Mason^{1,2}, C. J. Chiu³, R. J. Hogan^{1,4}, D. Moisseev^{5,6}, S. Kneifel⁷

¹Department of Meteorology, University of Reading, Reading, UK

²National Centre for Earth Observation (NCEO), University of Reading, Reading, UK

³Colorado State University, Fort Collins, Colorado, USA

⁴European Centre for Medium-range Weather Forecasts (ECMWF), Reading, UK

⁵Institute for Atmospheric and Earth System Research/Physics, Faculty of Science, University of Helsinki, Finland

⁶Finnish Meteorological Institute, Helsinki, Finland

⁷Institute of Geophysics and Meteorology, University of Cologne, Cologne, Germany

Key Points:

- The CAPTIVATE optimal estimation retrieval algorithm is applied to zenith-pointing Doppler cloud radars deployed during the Biogenic Aerosols—Effects on Clouds and Climate field campaign (BAECC 2014), in Hyytiälä, Finland.
- Doppler velocity is exploited to retrieve a parameter that modulates the mass, area and radar backscatter cross-sections to represent the continuum of particle morphologies from unrimed aggregates to graupel and hail.
- The retrieval provides insights into microphysical processes including aggregation and riming. Retrieved particle density is correlated with the availability of super-cooled liquid water, demonstrating potential to use the retrieval to diagnose embedded layers of mixed-phase clouds.

Corresponding author: S. L. Mason, s.l.mason@reading.ac.uk

Abstract

Retrievals of ice and snow are made from Ka- and W-band zenith-pointing Doppler radars at Hyytiälä, Finland, during the snow experiment (SNEX) component of the Biogenic Aerosols: Effects on Clouds and Climate (BAECC 2014) field campaign. In a novel optimal estimation retrieval, mean Doppler velocity is exploited to retrieve a “density factor” parameter which modulates the mass, shape, terminal velocity and backscatter cross-sections of ice particles. In a case study including aggregate snow and graupel we find that snow rate and ensemble mean ice density can be retrieved to within 50 % of in-situ measurements at the surface using dual-frequency Doppler radar retrievals. While Doppler measurements are essential to the retrieval of particle density, the dual-frequency ratio provides a strong constraint on particle size. The retrieved density factor is strongly correlated with liquid water path, indicating that riming is the primary process by which the density factor is modulated. Using liquid water path as a proxy for riming, profiles classified as unrimed snow, rimed snow and graupel exhibit distinct features characteristic of aggregation and riming processes, suggesting the potential to make estimates of process rates from these retrievals. We discuss the potential application of the technique to future satellite missions.

1 Introduction

Estimates of the global volume and distribution of snow are critical to understanding the atmospheric water budget and surface hydrology. While the first generation of spaceborne cloud and precipitation radars has greatly improved the detection of snow, remote-sensed estimates of snow mass flux and its microphysical properties remain highly uncertain. Understanding the microphysics of snow production within ice clouds is also critical to global rainfall: CloudSat 94-GHz radar [Stephens *et al.*, 2002] observations reveal that 85–90% of all precipitation events in the extratropics and poles originate in the ice phase, and that 34–40% of rain events in the subtropics and tropics fall from melting ice [Field and Heymsfield, 2015]. CloudSat snow retrievals [e.g. Liu, 2008; Kulie and Bennartz, 2009] have enabled the first remote-sensed estimates of snow over remote polar regions [Palerme *et al.*, 2014], and surveys of snow regimes [Chen *et al.*, 2016; Kulie *et al.*, 2016], but further microphysical insights are anticipated from upcoming satellite missions. The first of a second generation of satellite radars is the dual-frequency precipitation radar (DPR) aboard the global precipitation measurement mission [GPM; Hou *et al.*, 2014]; however, initial comparisons suggest DPR detects only about one-third of the mass of snow seen by CloudSat, concen-

54 trated in the heaviest 5% of snow events [*Casella et al.*, 2017]. Work is ongoing to better
55 evaluate remote-sensed snow rate at the surface [e.g. *Heymsfield et al.*, 2016] with the aim of
56 reducing uncertainties in retrievals from current satellite capability and informing the design
57 of future satellite sensors.

58 Remote-sensing of ice and snow requires knowledge of the morphology of ice par-
59 ticles, which may be any combination of pristine ice crystals grown by vapour deposition,
60 aggregates or fragments formed from interactions between ice particles, or rimed particles
61 and graupel having collected liquid drops in mixed-phase cloud. While a majority of snow
62 is assumed to fall as aggregate snowflakes [*Langleben*, 1954], the masses and fallspeeds of
63 ice particles remain fundamental to uncertainties in radar retrievals [*Hiley et al.*, 2011]. Ice
64 particle properties are especially uncertain in and below mixed-phase clouds, which are com-
65 mon in the extratropics and poles [*Hogan et al.*, 2003, 2004; *Cesana et al.*, 2012], radiatively
66 important in the polar regions and extratropics [e.g. *Shupe et al.*, 2004], imperfectly detected
67 by spaceborne radar and lidar [e.g. *Ceccaldi et al.*, 2013], and poorly represented in models
68 [e.g. *Tan et al.*, 2016]. Studies at ground stations have attributed 40% or more of the mass of
69 snow to rimed ice [*Harimaya and Sato*, 1989; *Mitchell et al.*, 1990; *Moisseev et al.*, 2017],
70 suggesting large uncertainties in remote-sensed estimates of snow rate while riming goes
71 undiagnosed, and riming has been strongly associated with heavy accumulation events in
72 mountainous regions [*Grazioli et al.*, 2015]. Remote-sensed estimates of snow stand to be
73 improved by the capability to diagnose riming in mixed-phase clouds, hence to better esti-
74 mate ice particle properties and the mass flux of snow.

75 Recent ground-based measurement campaigns have facilitated studies of snow micro-
76 physics using deployments of advanced radars, lidars and passive remote-sensors co-located
77 with in situ measurements of snow particles [e.g. *Szyrmer and Zawadzki*, 2014; *Petäjä et al.*,
78 2016]. Combined particle imaging and snow gauge instruments have enabled the quantifi-
79 cation of ice bulk density and rime mass [*Tiira et al.*, 2016; *Moisseev et al.*, 2017; *von Ler-*
80 *ber et al.*, 2017; *Grazioli et al.*, 2015], building upon previous studies characterising particle
81 morphologies and degrees of riming [e.g. *Harimaya and Sato*, 1989; *Mitchell et al.*, 1990].
82 These campaigns provide opportunities to evaluate and intercompare the representation of
83 ice and mixed-phase microphysics used in numerical models [*Lin et al.*, 2011; *Morrison and*
84 *Milbrandt*, 2015; *Morrison et al.*, 2015], as well as of ice particle morphology and growth
85 processes as they relate to radar backscatter [*Kneifel et al.*, 2011; *Leinonen and Szyrmer*,
86 2015]. Triple-frequency radar measurements have allowed for the evaluation of particle mod-

87 els using the signatures of rimed and unrimed ice particles [*Kneifel et al.*, 2015; *Stein et al.*,
88 2015], a technique that has recently been applied to colocated CloudSat and GPM measure-
89 ments [*Yin et al.*, 2017]. With Doppler radar capability, the morphology of snow can also be
90 inferred from terminal velocities of particles to estimate the degree of riming [*Mosimann*,
91 1995] or the density of rimed aggregates [*Szyrmer and Zawadzki*, 2014; ?], and it is possible
92 in some cases to distinguish ice from cloud droplets using Doppler spectra in mixed-phase
93 cloud [*Kalesse et al.*, 2016]. Recent ground-based remote-sensing and in situ measurement
94 campaigns have demonstrated the application of Doppler and multiple-frequency radar ob-
95 servations to improved retrievals of snow and riming.

96 In this study we demonstrate the novel retrieval of the properties of snow particles us-
97 ing vertically-pointing dual-frequency Doppler radars at Hyytiälä, Finland. Mean Doppler
98 velocity, a measure of the terminal velocity of hydrometeors, is used to estimate a parameter
99 that modulates the properties of ice particles along a continuum from unrimed aggregates
100 to graupel and hail. The retrieval is carried out within the optimal estimation framework for
101 Cloud Aerosol and Precipitation from mulTiple Instruments using a VAriational TEchnique
102 (CAPTIVATE), which provides the flexibility to assimilate observed variables from a range
103 of ground-based instruments. We consider the contribution of Doppler velocity and dual-
104 frequency radar reflectivity measurements to the retrieval, and compare against retrievals in
105 which particle density does not vary. The retrieved snow rate, particle size distribution and
106 bulk density are evaluated against in-situ measurements at the surface. This method for es-
107 timating ice particle morphology from mean Doppler velocity should be applicable to the
108 network of ARM and Cloudnet [*Illingworth et al.*, 2007] “supersites” with multi-frequency
109 Doppler radars, as well as to the upcoming ESA/JAXA Earth Cloud Aerosol Radiation Ex-
110 plorer [EarthCARE; *Illingworth et al.*, 2015], which will feature the first spaceborne Doppler
111 cloud radar in synergy with lidar and radiometers. In addition to Doppler capability, space-
112 borne multiple-frequency cloud radars have long been of interest to further improve global
113 observations of ice clouds and snow [*Hogan and Illingworth*, 1999; *Tanelli et al.*, 2009; *Löh-
114 nert et al.*, 2011; *Leinonen and Szyrmer*, 2015; *National Academies of Sciences Engineering
115 and Medicine*, 2018].

116 The paper is structured as follows: we describe the components of the CAPTIVATE
117 retrieval framework pertinent to estimates of ice and snow from radar measurements, with
118 a focus on formulating a new parameter with which to represent ice particles over a range
119 of densities from unrimed aggregates to graupel and hail (Section 2), and lay out the mea-

120 surements and atmospheric state data used for the present study (Section 3). We then present
 121 the results of retrievals for a case study of a frontal snow event with significant riming (Sec-
 122 tion 4.1), and a statistical evaluation of a retrieval of 10 snow events over a 2 month observa-
 123 tion period (Section 4.2). In our concluding remarks we consider applications of the retrieval
 124 to future satellite radar missions (Section 5).

125 **2 Retrieval framework**

126 The CAPTIVATE retrieval framework [Mason *et al.*, 2017] has been developed for
 127 radar–lidar–radiometer synergy retrievals from EarthCARE [Illingworth *et al.*, 2015]. CAP-
 128 TIVATE therefore includes instrument forward-models for the Doppler radar and high-spectral
 129 resolution lidar aboard EarthCARE, but is also designed to be easily configurable for active
 130 and passive sensors on ground-based and airborne platforms. Here we focus on the retrieval
 131 of snow from zenith-pointing ground-based radar measurements. The retrieval of ice and
 132 snow builds upon the methods employed for the synergy of CloudSat/CALIPSO observations
 133 [Delanoë and Hogan, 2008, 2010]; the novelty of the present retrieval is the availability of
 134 Doppler velocity measurements.

135 **2.1 Cost function and minimization**

136 The retrieval operates on a column-by-column basis to make an optimal estimate of the
 137 vector of state variables \mathbf{x} that best explains the observed variables \mathbf{y} within the bounds of
 138 prior expectations and measurement uncertainties [Rodgers, 2000]. The optimal estimate is
 139 that which minimizes the cost function

$$J = \frac{1}{2} \delta \mathbf{x}^\top \mathbf{B}^{-1} \delta \mathbf{x} + \frac{1}{2} \delta \mathbf{y}^\top \mathbf{R}^{-1} \delta \mathbf{y} + J_c(\mathbf{x}), \quad (1)$$

140 where $\delta \mathbf{x} = \mathbf{x} - \mathbf{x}_a$ is the difference between the state vector and its prior, and \mathbf{B} the er-
 141 ror covariance matrix of the priors; $\delta \mathbf{y} = \mathbf{y} - H(\mathbf{x})$ is the difference between the observed
 142 variables and the forward-modelled observations $H(\mathbf{x})$, and \mathbf{R} the error covariances of the
 143 observations and forward models; and $J_c(\mathbf{x})$ optionally applies regularization constraints to
 144 the vertical profile of the state vector [Twomey, 1977]. By quantifying uncertainties in the
 145 prior estimates of the state, measurement errors, and uncertainties in the implementation of
 146 the forward-models, the retrieval yields a robust best-estimate of the state variables and their
 147 associated error uncertainties. The cost function is minimized by iterating on the state vec-
 148 tor from the prior in the direction of the first and second derivatives of the cost function [the

149 Levenberg-Marquadt method; *Rodgers, 2000*]. The derivatives are computed efficiently and
 150 transparently using the combined array and automatic differentiation C++ software library,
 151 Adept [*Hogan, 2014, 2017*].

The vectors of state variables through the vertical profile \mathbf{x}_i for n classes of hydrometeor are retrieved from the observed variables \mathbf{y}_j of m instruments:

$$\mathbf{x} = \begin{pmatrix} \mathbf{x}_1 \\ \mathbf{x}_2 \\ \vdots \\ \mathbf{x}_n \end{pmatrix}, \quad \mathbf{y} = \begin{pmatrix} \mathbf{y}_1 \\ \mathbf{y}_2 \\ \vdots \\ \mathbf{y}_m \end{pmatrix}.$$

152 Both the selection of appropriate state variables for ice particles (Section 2.3) and the for-
 153 mulation of a radar forward-model for the observed variables (Section 2.4) depend on an
 154 underlying physical representation of ice particles: their size distribution, shape and mass,
 155 and their terminal fallspeeds.

156 2.2 Representation of ice particle properties

157 The bulk quantities of primary interest for remote-sensing are related to integrals over
 158 the particle size distribution (PSD; $N(D)$) with the average properties of ice particles, as a
 159 function of maximum particle dimension D . Unless stated otherwise, SI units are used. The
 160 ice water content (IWC) requires the mass of ice particles, $m(D)$:

$$IWC = \int_0^{\infty} m(D) N(D) dD, \quad (2)$$

161 while the mass flux or snow rate also includes particle terminal velocities, $v(D)$:

$$S = \int_0^{\infty} v(D) m(D) N(D) dD. \quad (3)$$

162 A characteristic bulk density of ice particles can be calculated as a volume flux-weighted
 163 density:

$$\bar{\rho} = \frac{\int_0^{\infty} m(D) v(D) N(D) dD}{\frac{\pi}{6} AR \int_0^{\infty} D^3 v(D) N(D) dD} \quad (4)$$

164 where AR is the aspect ratio of a horizontally-aligned oblate spheroid enclosing the parti-
 165 cle. A volume flux-weighted density for ease of comparison with estimates derived from in
 166 situ measurements of accumulation with a snow gauge [e.g. *Moisseev et al., 2017; von Ler-*
 167 *ber et al., 2017*]. While integrated quantities such as snow rate are especially sensitive to
 168 the formulation of the mass-size relation [*Heymsfield et al., 2010; Delanoë et al., 2014*], in

169 this study it will also be important to relate the mass and shape of particles to their terminal
 170 velocity in order to retrieve the morphology of snow particles from Doppler radar measure-
 171 ments.

172 In the following sections we first describe the PSD (Section 2.2.1), then the mass-size
 173 (Section 2.2.2) and area-size (Section 2.2.3) relations for a range of ice particles, and finally
 174 how particle properties are combined to estimate terminal fallspeeds (Section 2.2.4).

175 **2.2.1 Particle size distribution**

176 The PSD is represented as a normalized spectrum of the form

$$N(D) = N_w F(D/D_0). \quad (5)$$

177 where N_w is the normalized number concentration, D_0 is the median volume diameter [*Testud et al.*, 2001], and the function $F(D/D_0)$ can be either that of the normalized gamma dis-
 178 tribution [*Testud et al.*, 2001; *Illingworth and Blackman*, 2002; *Delanoë et al.*, 2005], or the
 179 universal modified gamma distribution derived by *Field et al.* [2005] for extratropical ice
 180 clouds [see also *Field et al.*, 2007; *Delanoë and Hogan*, 2008]. The normalized number con-
 181 centration can be estimated from the moments of the PSD:
 182

$$N_w = M_2^4 / M_3^3 \quad (6)$$

183 where M_n is the n^{th} moment. When using the gamma function a constant shape parameter
 184 of $\mu = 2$ is assumed in order to simplify the representation of the PSD; the shape parameter
 185 makes the smallest contribution to uncertainties in the retrieved ice water content [*Delanoë et al.*, 2005]. In practice for the present study, the differences between the retrieved quantities
 186 using the normalized gamma and *Field et al.* [2005] PSD were found to be within the uncer-
 187 tainty of the retrievals; in the results presented here the *Field et al.* [2005] PSD is used unless
 188 otherwise stated.
 189

190 **2.2.2 Mass-size relations**

191 Ice particle mass is expressed as a function of maximum dimension by the power law

$$m(D) = a_m D^{b_m}, \quad (7)$$

192 where the prefactor a_m scales the density of ice at all sizes, and the exponent b_m controls the
 193 size-dependence of particle mass and is related to the particle growth mechanism or shape

194 of the particle. Aggregate snowflakes have exponents around $b_m = 2$, close to the theoretical
 195 value for fractals [Westbrook *et al.*, 2004; Stein *et al.*, 2015]. More rounded graupel and hail
 196 particles have exponents closer to $b_m = 3$, the physical maximum for spheres [Leinonen and
 197 Moisseev, 2015].

198 While snow particles are observed to vary greatly in morphology, the majority of snow
 199 is thought to fall as aggregate snowflakes [Langleben, 1954]—indeed, the mass-size rela-
 200 tions used for ice and snow tend to be derived from measurements dominated by unrimed
 201 aggregates. We follow the approach of Hogan *et al.* [2012], who showed that in-situ mea-
 202 surements of cirrus were consistent with radar reflectivities when the mass-size relation de-
 203 rived for “aggregates of unrimed bullets, columns and side-planes” by Brown and Francis
 204 [1995] was used. In this representation the smallest particles are assumed to be solid quasi-
 205 spheroidal ice crystals, while larger aggregates occupy the volume of a horizontally-aligned
 206 oblate spheroid with an aspect ratio—that between the minimum (vertical) dimension and the
 207 maximum (horizontal) dimension—of $AR = 0.6$. Hogan *et al.* [2012] found that this value
 208 provided a good fit to a database of aircraft measurements as well as other studies in the liter-
 209 ature. Combining dual-polarization weather radar and surface based snowfall measurements
 210 at Hyytiälä, [Li *et al.*, 2018] found that the aspect ratio varies with riming fraction between
 211 0.4 and 0.9, while analysis of PIP images by Tiira *et al.* [2016] yielded a median aspect ratio
 212 of 0.72. However, the applicability of particle images to derive particle geometrical prop-
 213 erties was questioned by Jiang *et al.* [2017]; hence, Tiira *et al.* [2016] also used a single as-
 214 pect ratio value of 0.6 for density retrievals. In the present study it was found that assuming
 215 $AR = 0.8$ instead of $AR = 0.6$ led to an increase in retrieved ice water content of approxi-
 216 mately 20 %, demonstrating that the shape and orientation of ice particles is an important
 217 uncertainty in the remote-sensing of snow [see also Hogan and Westbrook, 2014].

218 How does riming affect the mass-size relation of snow? Numerical analogues for “bal-
 219 listic” collisions between ice particles (aggregation) and between ice particles and super-
 220 cooled liquid drops (riming) suggest that aggregating particles will retain mass-size expo-
 221 nents around $b_m = 2$, while those growing by riming will tend toward exponents of $b_m = 3$
 222 [Jullien, 1992]. A conceptual model for riming introduced by Heymsfield [1982] proposes a
 223 two stage process for the riming of aggregate snowflakes [see also Morrison and Milbrandt,
 224 2015; Moisseev *et al.*, 2017], in which an aggregate is first “filled in” by freezing supercooled
 225 drops, increasing the mass of the particle but not its size: this increases the prefactor of the
 226 mass-size relation while the exponent remains close to $b_m = 2$ [e.g. Szyrmer and Zawadzki,

227 2014; *Morrison and Milbrandt, 2015; Moisseev et al., 2017; von Lerber et al., 2017*]. That
 228 the first stage of riming does not scale the exponent of the mass-size relation is consistent
 229 with earlier studies of rimed snow [e.g. *Harimaya and Sato, 1989; Mitchell et al., 1990*].
 230 Once the particle geometry is closed by in-filling, it is classified as graupel. In this second
 231 stage rime is accreted to the outside of the particle, adding to both its mass and diameter, and
 232 as the particles become rounder in shape the exponent approaches $b_m = 3$ [*Mitchell, 1996*].
 233 The morphology of an ice particle encodes a history of multiple and interacting processes,
 234 including aggregation and transitions between stages of riming, which may be observed mi-
 235 croscopically [*Fujiyoshi and Wakahama, 1985*] or tracked within a microphysical parame-
 236 terization scheme [*Morrison et al., 2015; Morrison and Milbrandt, 2015*], but are unlikely to
 237 be instantaneously grasped by remote sensing. In a modelling study *Leinonen and Szyrmer*
 238 [2015] compared particles that have grown first by aggregation then riming to those that have
 239 grown by simultaneous aggregation and riming. While it was found that aggregation and
 240 riming, whether in series or in parallel, form particles that are indistinguishable in terms of
 241 radar backscatter—an important result for remote-sensing—the corresponding mass-size re-
 242 lations were distinct: when riming followed aggregation the exponent was found to remain
 243 close to $b_m = 2.1$ until a relatively high degree of riming; but when riming and aggrega-
 244 tion were simultaneous the exponent varied significantly even at low degrees of riming. This
 245 complicates the two-stage conceptual model of riming. While we may attempt to formulate a
 246 representation of the range of morphologies and densities of ice particles for remote-sensing
 247 applications, the possibility of multiple interacting ice processes means we should be cau-
 248 tious about attributing all variations in particle density to riming.

249 It has been observed that the mass-size relations derived from studies of snow and ice
 250 form a continuum of ice particles from unrimed snowflakes to graupel and hail [*Lin and*
 251 *Colle, 2011*]; Fig. 1 shows the mass-size prefactors and exponents a_m and b_m in cgs units
 252 and converted where necessary into terms of maximum particle dimension D . Particles with
 253 low mass-size prefactors and exponents—in the lower left part of the diagram—include a
 254 range of unrimed aggregates, as well as other low-density species such as dendrites, needles
 255 and columns. Measurements of unrimed snow from ground-based studies [*Tiira et al., 2016;*
 256 *von Lerber et al., 2017*] are consistent with aircraft studies of ice clouds [*Heymsfield and*
 257 *Westbrook, 2010; Brown and Francis, 1995*], with b_m varying between 1.9 and 2.1. Larger
 258 mass-size prefactors and exponents—in the centre to the upper-right part of the diagram—
 259 include denser or more compact particles of various kinds, often with some degree of rim-

260 ing. Exponents for rimed aggregates and low-density graupel are between 2.1 and 2.4 [*Er-*
 261 *fani and Mitchell, 2017; von Lerber et al., 2017*]; while for lump graupel and hail classifi-
 262 cations [*Mitchell, 1996; Mace and Benson, 2017; Zikmunda and Vali, 1972*] the exponent
 263 approaches 3.0. We note that the position on the mass-size relation diagram is not solely
 264 related to the effect of riming, especially for slender 1- and 2-dimensional species such as
 265 columns and dendrites: for example, the rimed dendrites in *Erfani and Mitchell [2017]* have
 266 a lower mass-size exponent than the unrimed dendrites; and the different sizes of hexagonal
 267 columns in *Mitchell [1996]* range from the upper-right part of the diagram for the smallest
 268 columns, to the extreme lower-left for the largest.

275 Variations in ice particle density have been parameterized in many ways. Fixed den-
 276 sities can be assumed depending on the cloud type, with low-density aggregates in strati-
 277 form cloud and graupel-like particles in convective cloud [e.g. *Greco et al., 2016*]. *Lin et al.*
 278 [*2011*] parameterize ice density according to temperature. *Szyrmer and Zawadzki [2014]*
 279 demonstrate a radar retrieval of lightly rimed snow from ground-based dual-frequency Doppler
 280 radars in which the prefactor a_m is scaled to increase the density of ice due to riming, while
 281 the exponent is fixed at $b_m = 2$. Similarly, *Moisseev et al. [2017]* represented the density of
 282 snow by scaling the prefactor of the mass-size relation and holding the exponent constant.

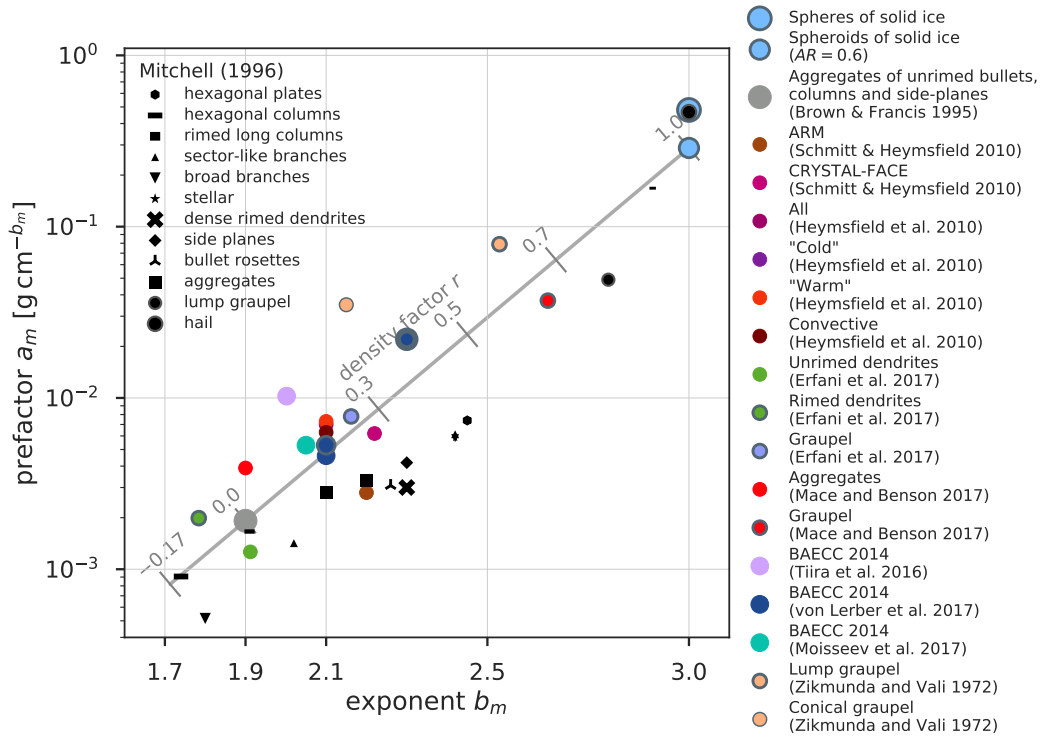
283 In order to represent a continuum of ice particles from unrimed and rimed aggregates
 284 to graupel and hail, we parameterize particle mass based on a “density factor” r (grey line
 285 in Fig. 1) that is continuous between the mass-size relation for the unrimed aggregates of
 286 *Brown and Francis [1995]* ($m = 0.0121 D^{1.9}$ kg where $r = 0$) and that of oblate spheroids of
 287 solid ice ($m = 288 D^3$ kg at $r = 1$). The parameterized exponent varies linearly with density
 288 factor between these two reference points ($b_m = 1.9$ and $b_m = 3$):

$$b'_m(r) = 3r + 1.9(1 - r), \quad (8)$$

289 while the prefactor is scaled according to the requirement that particle masses are equivalent
 290 for all r at some critical diameter D_c , which can be calculated as $(0.0121/288)^{1/(3-1.9)} = 105 \mu\text{m}$,
 291 similar to the transition from quasi-spheroids to aggregates in *Hogan et al. [2012]*. Normal-
 292 izing by the critical diameter, the mass-size relation for all particles can be expressed

$$m(D, r) = a'_m \left(\frac{D}{D_c} \right)^{b'_m}, \quad (9)$$

293 where the normalized prefactor $a'_m = a_m D_c^{b_m} = 33.3 \mu\text{g}$ is the particle mass at the critical
 294 diameter. A similar normalized mass-size relation was employed in *Szyrmer and Zawadzki*



269 **Figure 1.** A comparison of $m(D)$ power-law prefactors and exponents. Coloured circles show a_m, b_m for
 270 various studies of ice and snow. Black markers correspond to particle types summarized in Mitchell [1996];
 271 where multiple markers of a particular type are shown, their relative size indicates the size range for which
 272 the mass-size relation was derived. Unrimed aggregates [Brown and Francis, 1995] and spheroids of solid
 273 ice define the mass-size relation as a function of density factor r : the grey line indicates the values of a_m, b_m
 274 parameterized by the density factor in the range $-0.17 < r < 1.0$.

295 [2014] [see also *Maahn et al.*, 2015; *Maahn and Löhnert*, 2017], but in that study the criti-
 296 cal diameter was selected to be close to the median particle diameter to minimize the effect
 297 of fixing the exponent of the mass-size relation $b_m = 2$. In the present retrieval all particles
 298 smaller than the critical diameter are assumed to be solid quasi-spheroids; expressed another
 299 way, the fractional volume of a particle occupied by ice is given by the ice fraction,

$$f(D, r) = \begin{cases} 1.0 & D \leq D_c \\ (D/D_c)^{b'_m-3} & D > D_c \end{cases} \quad (10)$$

300 The ice fraction-size relation for a range of density factors is shown in Fig. 3.

301 In terms of the density factor, the unrimed and lightly-rimed snow correspond to low
 302 values ($r < 0.3$), and heavily-rimed snow and graupel [*von Lerber et al.*, 2017; *Mace and*
 303 *Benson*, 2017] relate to higher values ($0.3 < r < 0.7$). While $r = 1$ is the upper limit, small
 304 negative density factors are possible, and allow for the representation of particles with lower
 305 densities such as dendrites [*Erfani and Mitchell*, 2017] or large hexagonal columns [*Mitchell*,
 306 1996].

307 We note that the density factor is not intended to explicitly represent the effect of the
 308 riming process on the mass of a particle, but allows for a smooth transition between unrimed
 309 and rimed aggregates to graupel and hail which we hope will be sufficient to allow an esti-
 310 mate of ice morphology based on particle fallspeeds. The density factor pivots the mass-size
 311 relation of ice particles larger than the critical diameter (Fig. 3), but without representing
 312 the transition features that would correspond to the multiple stages of riming. A more
 313 process-oriented parameterisation of the “in-filling” stage of rimed aggregate snowflakes
 314 would be to scale the mass-size prefactor with the density factor, while the exponent re-
 315 mains constant. While this would better represent the conceptual model of the riming pro-
 316 cess, it would not encompass the observed variability in the mass-size relations of unrimed
 317 snowflakes, or the transition to graupel-like particles. A comparison of the two parameterisa-
 318 tions indicated that the retrieval was not strongly sensitive to the representation of the density
 319 factor, especially for estimates of unrimed to moderately rimed aggregates. With additional
 320 observational evidence, a more complex representation of the effects of riming on particle
 321 morphology—including expected changes in the masses and shapes of particles during dif-
 322 ferent stages of riming—may allow for improved retrievals and better quantified uncertain-
 323 ties. This should be the subject of future work.

2.2.3 Area-size relation

Similar to the mass-size relation, the cross-sectional area of ice particles is expressed as a power law:

$$A = a_A D^{b_A}. \quad (11)$$

The area-size relation of unrimed aggregates is derived from the mass-size [Brown and Francis, 1995] and mass-area relations [Francis et al., 1998] from aircraft measurements of cirrus clouds $A = 0.02038 D^{1.624} \text{ m}^2$ in SI units and in terms of maximum dimension. The geometric upper limit for horizontally-aligned oblate spheroids with maximum dimension on the horizontal plane is $A = \pi/4 D^2 \text{ m}^2$. A comparison of area-size relations from a range of studies (Fig. 2) again shows a relationship between the prefactors and exponents across particle types: lower density factors are consistent with unrimed ice particles [Schmitt and Heymsfield, 2010; Mace and Benson, 2017], and larger density factors with rimed particles [Heymsfield and Kajikawa, 1987], graupel and hail [Mitchell, 1996]. While increases in cross-sectional area are consistent with the conceptual model of riming leading to the infilling of aggregates and a transition to rounded graupel-like particles, there is significant variability between particle types: for example, columns may retain low cross-sectional areas despite riming, while riming may have little effect on the cross-sectional area of plates.

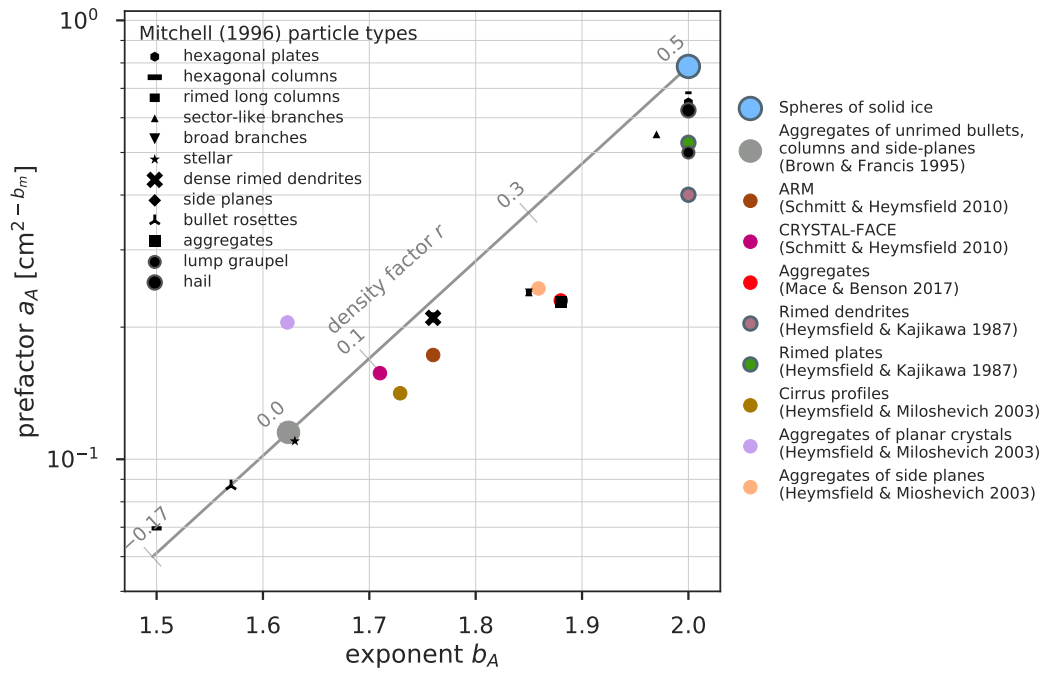
To represent the increased cross-sectional area of rimed aggregates and graupel, we scale the area-size relation by the density factor r ; however, to represent the more rounded shapes of heavily rimed aggregates and graupel, the cross-sectional area is maximized for $r = r_{\text{max}}$, so that

$$b'_A = 2 \frac{r}{r_{\text{max}}} + 1.624 \left(1 - \frac{r}{r_{\text{max}}}\right). \quad (12)$$

The prefactor is scaled by a critical diameter D_{c_A} , the size at which the cross-sectional area of unrimed aggregates and spheres are equal, which can be calculated to be $61 \mu\text{m}$. The normalized area-size relation is therefore

$$A = a'_A \left(\frac{D}{D_{c_A}} \right)^{b'_A} \quad (13)$$

where the modified prefactor is the area at the critical diameter $a'_A = a_A D_{c_A}^{b'_A}$. Most rimed and unrimed aggregates correspond to density factors $r < 0.3$, while quasi-spheroidal and heavily rimed particles, graupel and hail have $r \approx r_{\text{max}}$. A marginally more complex area-size relation that better fits the observations would be to allow both the prefactor and exponent to vary for $r < r_{\text{max}}$, before scaling only the prefactor up to $r = 1$.



340 **Figure 2.** A comparison of power law prefactors and exponents for ice particle area-size relations.
 341 Coloured circles show a_A, b_A derived from a range of aircraft and surface studies. Black markers corre-
 342 spond to specific particle types summarized in *Mitchell* [1996]. The parameterized area-size relation, which
 343 varies with density factor between unrimed aggregates [$r = 0$ *Brown and Francis, 1995; Francis et al., 1998*]
 344 and spheres of solid ice ($r = r_{\max}$), is shown with a grey line.

357 Particle area is often expressed as the area ratio, which is the cross-sectional area of the
 358 particle normalized by area of the circumscribing circle, or

$$A_r(D) = \begin{cases} 1.0 & D \leq D_{cA} \\ (D/D_{cA})^{b'_A-2} & D > D_{cA} \end{cases} . \quad (14)$$

359 **2.2.4 Velocity-size relation**

360 The boundary layer or hydrodynamic method provides an estimate of the terminal ve-
 361 locity of a hydrometeor based on size, area ratio and mass [e.g. *Mitchell, 1996; Mitchell and*
 362 *Heymsfield, 2005; Khvorostyanov and Curry, 2005; Heymsfield and Westbrook, 2010*] or
 363 conversely, an estimate of particle mass from measured diameter, cross-sectional area and
 364 fallspeed [e.g. *von Lerber et al., 2017*]. In the previous sections the mass- and area-size re-
 365 lations for ice particles were expressed as functions of diameter and density factor; hence a
 366 look-up table for particle terminal velocities is produced using the method of *Heymsfield and*
 367 *Westbrook [2010]*.

372 The terminal fallspeed of ice particles $v(D, f)$ for a range of maximum dimensions and
 373 ice fractions (see eq. 10) is overlaid with curves corresponding to the mass-size relations for
 374 a range of density factors (Fig. 3). As the mean Doppler velocity relates to the reflectivity-
 375 weighted average of particle fallspeeds, the density factor has the greatest effect on the fall-
 376 speeds of the largest particles. While the largest unrimed aggregates do not exceed terminal
 377 velocities of 2 m s^{-1} , even low density factors effect significant increases in fallspeed for par-
 378 ticles of the same size.

379 **2.3 State variables**

380 **2.3.1 Extinction coefficient and primed number concentration**

381 The choice of retrieved state variables is flexible within CAPTIVATE, as are any ver-
 382 tical or temporal smoothing applied to the state variables. In this retrieval, a state variable
 383 related to the density factor is added to those used for retrievals of ice clouds from radar-
 384 lidar synergy described in *Delanoë and Hogan [2008, 2010]*. The first state variable is the
 385 visible extinction coefficient of ice in the geometric optics approximation, α_v . The second
 386 state variable is the primed number concentration,

$$N'_0 = N_w \alpha_v^{-0.6} \quad (15)$$

387 from which the normalized number concentration N_w from (5) can be recovered, since the
 388 extinction coefficient is also retrieved. *Delanoë and Hogan* [2008] showed using in situ air-
 389 craft data that this choice of state variables for ice allows for a convenient a priori estimation
 390 of the primed number concentration as a function of atmospheric temperature (Table. 1). An
 391 additional parameter, the lidar extinction-to-backscatter ratio, can also be retrieved in radar-
 392 lidar synergy applications; however, in this study we assume this variable is constant.

393 The minimization scheme does not limit the values of retrieved variables, so we formu-
 394 late state variables such that they remain physically meaningful at all values; this is achieved
 395 by using the natural logarithms of N'_0 and α_v .

396 While these choices of state variables for ice and snow are convenient for the reasons
 397 described above, they are not necessarily the most physically meaningful quantities. For
 398 comparison with in situ measurements, an integrated quantity such as the melted-equivalent
 399 snow rate, as well as the median diameter and normalized number concentration, are more
 400 convenient. As the extinction coefficient is an integral over the PSD and the primed number
 401 concentration relates to a parameter of the PSD by (15), the two state variables are sufficient
 402 to calculate the PSD.

403 **2.3.2 Density index**

404 The natural logarithm of the density factor is not a suitable state vector; the density
 405 factor should not exceed $r = 1$, but small negative values are physically meaningful. Instead
 406 we retrieve the density index r' , a state variable defined such that:

$$r = \frac{f(r' + r_0) + f(r_0)}{1 - f(r_0)}, \quad (16)$$

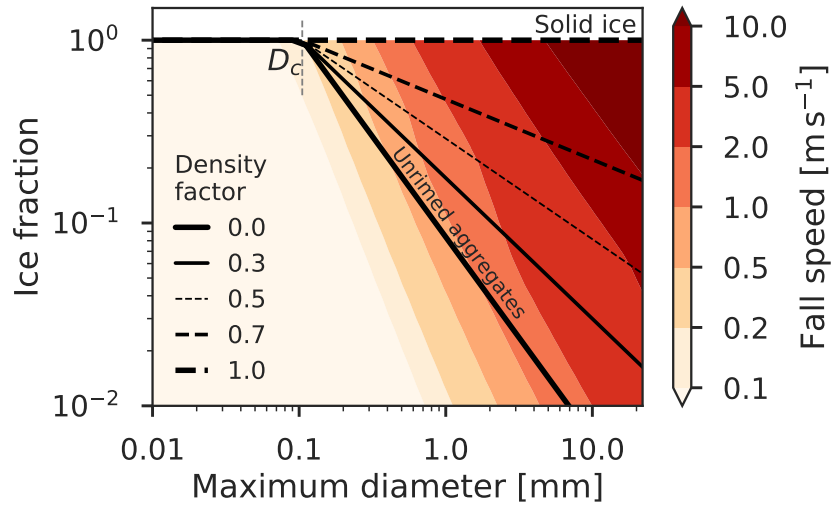
407 where

$$f(x) = \frac{1}{2} + \frac{\tan^{-1} x}{\pi} \quad (17)$$

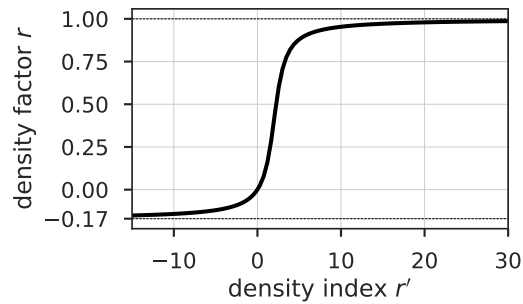
408 and $r_0 = -2$. This transform function has the property that $r = 0$ when $r' = 0$, and for any
 409 value of r' , r is within the range -0.173 to 1.0 . The transform is illustrated in Fig. 4.

413 **2.3.3 Representation of the state vector**

414 To reduce the effect of measurement noise on the retrieval, the profile of each state
 415 variable is represented as the basis functions of a cubic spline [*Hogan, 2007*]. The degrees of
 416 freedom of the retrieval can therefore be controlled by altering the spacing of the basis func-



368 **Figure 3.** The terminal fallspeeds $v(D, f)$ of ice particles as a function of maximum dimension D , and
 369 ice fraction f . Black lines correspond to the parameterized mass-size relations for density factors between
 370 unrimed aggregates ($r = 0$) and spheroids of solid ice ($r = 1$). D_c is the diameter below which all particles
 371 are represented as dense quasi-spheroidal particles.



410 **Figure 4.** The transform function between density index r' , the retrieved state variable, and the density
 411 factor which modulates the particle properties between unrimed aggregates at $r = 0$ and spheroids of solid ice
 412 at $r = 1$.

417 tions, which modifies the effective scales over which features are retrieved [Rodgers, 2000].
 418 A Kalman smoother [Rodgers, 2000] is applied to the extinction coefficient and density in-
 419 dex, so that the retrieval of these quantities is constrained by adjacent profiles. In the first
 420 pass of the smoother the retrieval is constrained by subsequent rays and, on the second pass,
 421 in both directions. For the retrieval of the density factor, this will have the effect of filtering
 422 out smaller-scale fluctuations in the mean Doppler velocity due to turbulent vertical air mo-
 423 tion.

The state vector for ice cloud and snow is therefore

$$\mathbf{x}_{\text{ice}} = \begin{pmatrix} \ln \alpha_v \\ \ln N'_0 \\ r' \end{pmatrix}.$$

424 The prior estimate of the state vector and associated uncertainties represent our knowledge
 425 of the state before the measurement vector is assimilated. The values and uncertainties of the
 426 priors, and the vertical representation of each state variable are summarized in Table 1; note
 427 that the uncertainties in the priors are in terms of the natural logarithm of the physical param-
 428 eters. From a large database of in situ measurements of ice clouds [Delanoë *et al.*, 2005] an
 429 expression has been derived for $\ln N'_0$ as a function of atmospheric temperature, with a vari-
 430 ance of 1.0 [Fig. 3b in Delanoë and Hogan, 2008], and a similar function of temperature is
 431 used for the prior extinction coefficient. When fewer observational variables are used it may
 432 be necessary to reduce the number of degrees of freedom by holding some state variables at
 433 their a priori values; these state variables can be represented within the retrieval as a “model”
 434 variable, wherein its value does not vary but its prior uncertainty is assimilated.

438 2.4 Observed variables and radar forward model

439 2.4.1 Reflectivity factor

440 The observed variables for each radar are the apparent radar reflectivity factor Z_f and
 441 mean Doppler velocity V_f at the radar frequency f . The reflectivity factor is given by

$$Z_f = 10^{18} \frac{\lambda^4}{\pi^5 |K_f|^2} \int_0^\infty \sigma_f(D) N(D) dD \quad (18)$$

442 where λ is the radar wavelength, K_f is the dielectric factor, and $\sigma_f(D)$ is the radar backscat-
 443 ter cross-section. Radar attenuation due to atmospheric gases is modelled from the atmo-
 444 spheric state using Liebe [1985], so that this effect is included in the observed and forward-
 445 modelled radar reflectivities.

435 **Table 1.** State variables for ice and snow, their priors, uncertainties and vertical representation. Note that
 436 we take as the state variables the natural logarithms of key parameters; stated uncertainties are therefore
 437 uncertainties in the natural logarithm of the priors.

State variable \mathbf{x}_i	Prior \mathbf{x}_i^a	Prior uncertainty $\sigma(\mathbf{x}_i^a)$	Cubic spline spacing [m]
Extinction coefficient $\ln \alpha_v$	$-9.2103 - 0.03148 T$ (where T is in $^{\circ}C$)	10.0	150
Primed number concentra- tion $\ln N'_0$	$23.03 - 0.12997 T$ (where T is in $^{\circ}C$)	1.0	600
Density index r'	0.0	1.0	150

446 Attenuation due to liquid water can be significant for millimetre-wavelength radars,
 447 and can either be accounted for by simultaneously retrieving the liquid water content, or by
 448 correcting for attenuation in the radar reflectivities prior to the retrieval. The former option
 449 is most suited to a radar–lidar–radiometer retrieval wherein the lidar backscatter and a visible
 450 radiance may provide adequate constraints; for a radar-only retrieval the available observed
 451 variables are dominated by ice, and the retrieval of liquid water content would be undercon-
 452 strained. Radar reflectivities can be pre-corrected for liquid attenuation based on an esti-
 453 mate of the liquid water path, such as from a microwave radiometer. In this study we follow
 454 the correction described in *Kneifel et al.* [2015]; the vertical distribution of SLW not being
 455 known, it is distributed evenly over the lowest 4 km of the atmosphere. Alternative correc-
 456 tions may be made by assuming all of the attenuation takes place below the lowest radar gate,
 457 or by locating the liquid in one or more shallow layers based on other evidence such as a re-
 458 cent sounding, or Doppler spectra [e.g. *Kalesse et al.*, 2016]. In practice we found that the
 459 uncertainty in W-band radar reflectivity between the different corrections was on the order
 460 of 1 to 2 dB; this can be accounted for within CAPTIVATE by increasing the observational
 461 uncertainty applied to the measurement vector (see Section. 2.4.4).

462 Reflectivity enhancement due to radar multiple scattering can be modelled using the
 463 method of *Hogan* [2008]; however, in this application with ground-based narrow beamwidth
 464 radars, we assume multiple scattering is negligible. The uncertainty in the radar reflectivity
 465 includes both observational and forward-model errors.

2.4.2 Mean Doppler velocity

Mean Doppler velocity is the reflectivity-weighted fallspeed of hydrometeors

$$V_f = \frac{\int_0^\infty v(D) \sigma_f(D) N(D) dD}{\int_0^\infty \sigma_f(D) N(D) dD}, \quad (19)$$

where $v(D)$ is corrected for air density, and positive values of mean Doppler velocity are toward the surface. The forward-modelled mean Doppler velocity neglects air motion, the effects of which are also included in the observational uncertainty. In the stratiform snow events in this study we assume that the mean Doppler velocity is dominated by the terminal velocities of hydrometeors rather than vertical air motions. In convective situations or where ice particles are very small, this assumption may not be justified, and would lead to a misdiagnosis of particle density; this will be considered in Section 4.1.

2.4.3 Scattering models

In addition to the density and shape of snow particles (Section 2.2), variability in particle morphology has a significant impact on the scattering of microwave radiation, which must be approximated within the radar forward-model. The self-similar Rayleigh-Gans approximation [SSRGA; *Hogan and Westbrook, 2014; Hogan et al., 2017*] provides an accurate estimate of the radar backscatter cross-section for unrimed aggregates, but underestimates the radar backscatter of higher-density rimed particles. Snow particles have often been approximated by “soft spheroids”—oblate spheroids composed of a homogenous mixture of ice and air—for which the radar backscatter can be estimated using the **T**-matrix method [e.g. *Hogan et al., 2012*]. *Leinonen and Szyrmer [2015]* found that soft spheroids provide a good approximation to the backscatter of dense graupel-like particles, but not to rimed aggregates. In both approximations particles are represented as occupying the volume of horizontally-aligned oblate spheroids with an aspect ratio of $AR = 0.6$ [*Hogan et al., 2012*].

In the absence of an explicit model for rimed aggregates, we represent the backscatter cross-section in the transition from unrimed aggregates to graupel as an external mixture between SSRGA ($r \leq 0.2$) and soft spheroids ($r \geq 0.5$). These thresholds were selected based on the ranges of density factors associated with mass-size relations for studies of unrimed aggregates and graupel (Fig. 1). As a check on this representation, the forward-modelled radar backscatter from a gamma distribution of particles was used to generate dual-wavelength ratios (DWRs) at Ka–W-bands and X–Ka-bands for a range of density factors (Fig. 5); these curves are overlaid with triple-frequency radar measurements from three snow events during

496 BAECC 2014 [Kneifel *et al.*, 2015, c.f. their Fig. 1]. A thin contour highlights the most fre-
 497 quent DWRs observed during the snow event that is studied in Section 4.1. The upright band
 498 of $DWR_{Ka-W} < 10$ dB and large DWR_{X-Ka} corresponds to the “hook” feature identified for
 499 unrimed aggregates, while the flat feature with low DWR_{X-Ka} is associated with denser
 500 graupel-like particles. The triple-frequency signatures represented by SSRGA ($r \leq 0.2$)
 501 resemble those of unrimed aggregates, while the soft spheroids ($r \geq 0.5$) fit the flatter sig-
 502 nature associated with graupel. This demonstrates that a simple hybrid representation at
 503 least qualitatively permits the signatures of unrimed aggregates and dense rimed particles in
 504 multiple-frequency radar observations—but does not necessarily address known limitations
 505 in the soft spheroid approximation for a range of dense particles [Leinonen and Szyrmer,
 506 2015; Hogan *et al.*, 2017]. The modelling and measurement of the morphology and multiple-
 507 frequency radar scattering of ice particles are of significant research interest [e.g. Kneifel
 508 *et al.*, 2018], and improved approximations for the backscatter cross-sections for rimed ag-
 509 gregates will both reduce uncertainties in the present retrieval, and allow for increased confi-
 510 dence in multiple-frequency radar retrievals of snow.

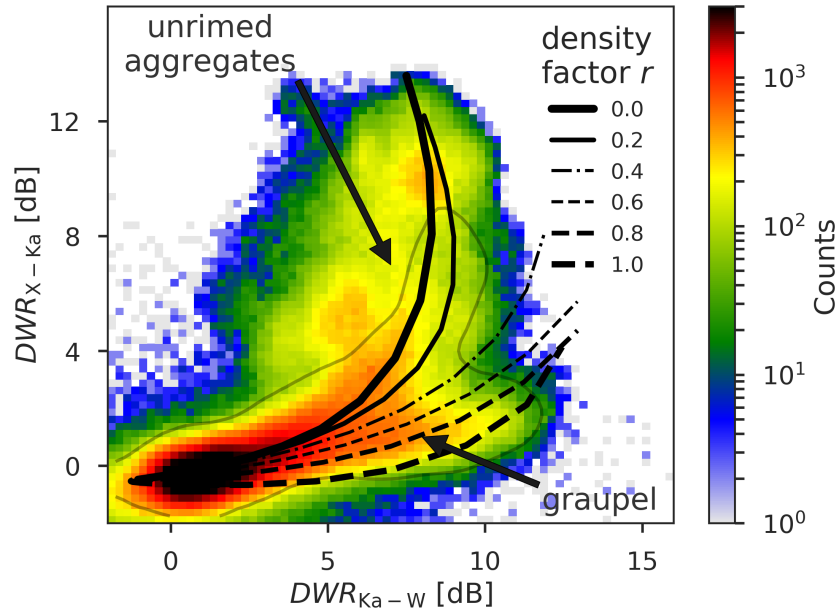
518 **2.4.4 Measurement vector**

The vector of observed variables for a dual-frequency Doppler radar retrieval is

$$\mathbf{y} = \begin{pmatrix} Z_{f_0} \\ V_{f_0} \\ Z_{f_1} \\ V_{f_1} \end{pmatrix}.$$

519 In principal more than two radar frequencies could be included in the measurement vector;
 520 and in practice, as discussed in the next section, some of the observed variables may not be
 521 assimilated in the present study.

522 The uncertainties in the measurement vector includes the stated measurement error for
 523 the instruments (Table 2), other sources of observational uncertainty, and an estimate of the
 524 uncertainties in the assumptions that form the basis of the instrument forward-model. For a
 525 retrieval that relies upon the mean Doppler velocity to estimate the properties of hydromete-
 526 ors, the treatment of and sensitivity to uncertainties in Doppler measurements are of partic-
 527 ular interest. For the present study we assume uncertainties of 3 dB in the radar reflectivities
 528 and 1.0 m s^{-1} in the mean Doppler velocity.



511 **Figure 5.** Joint histogram of measured dual-wavelength ratios (DWRs) for triple-frequency radar ob-
 512 servations from the three cases studied in *Kneifel et al.* [2015]; a thin contour encloses the most frequent
 513 measurements during the February 21–22 2014 case considered in Section 4.1, highlighting distinct features
 514 associated with aggregates and graupel. Black curves represent the forward-modelled DWR for an expo-
 515 nential distribution of particles with density factors from unrimed aggregates (using SSRGA for $r < 0.2$) to
 516 graupel (“soft spheroids” for $r > 0.5$); the transition between rimed aggregates and graupel is represented by
 517 an external mixture of the two approximations to the radar backscatter cross-section.

3 BAECC 2014 data

As part of the Biogenic Aerosols—Effects on Clouds and Climate field campaign [BAECC 2014; *Petäjä et al.*, 2016], the US Department of Energy atmospheric radiation measurement (ARM) program’s second mobile facility (AMF2) was deployed at the University of Helsinki’s Hyytiälä forestry field station (61°51’N, 24°17’E). The remote-sensing and in situ instrumentation, and their deployment are documented in *Kneifel et al.* [2015]. Between 1 February and 31 March 2014 the snowfall measurement experiment (SNEX) intensive observation period (IOP) focused on the measurement of snow microphysics. Remote-sensing observations include vertically-pointing Doppler radars, lidar and microwave radiometer instruments, and the state of the atmosphere from reanalysis (Section 3.1) will be evaluated against in situ measurements at the surface (Section 3.2).

3.1 Remote sensed measurements

Two vertically-pointing Doppler radars are the primary remote-sensing instruments in this study. The 35 GHz Ka-band Zenith Radar (KAZR) and the 95 GHz Marine W-band cloud radar (MWACR) were deployed at Hyytiälä during the SNEX IOP. Due to a mispointing of MWACR, mean Doppler velocity measurements from that radar are not used in this study. It is important that KAZR and MWACR sampling volumes are broadly overlapping; both radar measurements are resampled from approximately 2 s to 120 s. Calibration of MWACR and KAZR against a colocated vertically-pointing X-band radar is carried out as described in *Kneifel et al.* [2015], after accounting for attenuation due to atmospheric gases and liquid; when X-band radar is not available the most recent calibration is applied, and MWACR radar reflectivity is calibrated against KAZR radar reflectivity at cloud-top after correcting for attenuation.

Additional observations are available from the AMF2 high-spectral resolution lidar (HSRL), which measures molecular and particulate backscatter at 532 nm with gate spacing of 30 m and temporal resolution of 120 s. HSRL could be used for radar–lidar synergy retrievals of non-precipitating ice cloud, where the lidar provides valuable information on smaller ice particles and liquid droplets; however, in the rimed snow events of interest here the lidar is completely attenuated by liquid water near the surface. HSRL data are therefore presented alongside the radar data, but are not assimilated in the retrieval.

552

Table 2. AMF2 zenith-pointing radar instruments and observational uncertainties

Instrument	KAZR	MWACR
Frequency	35 GHz	95 GHz
Wavelength	8.6 mm	3.2 mm
Gate spacing	30 m	30 m
Beam width	0.38 °	0.3 °
Reflectivity uncertainty	1 dB	1 dB
Mean Doppler velocity uncertainty	0.5 m s ⁻¹	n/a

560

561

562

563

564

565

566

Microwave radiometer (MWR) measurements at 23.8 and 31.4 GHz are used to retrieve liquid water path (LWP) and water vapour path [Cadeddu *et al.*, 2013]. While microwave radiometer measurements are not included in the retrieval, estimates of LWP provide information on the magnitude of supercooled liquid water (SLW) that are used to correct for radar attenuation due to liquid (discussed above and in Section 2.4) and to provide context for the retrieval of riming based on the availability of supercooled liquid water in mixed-phase clouds [e.g. Kalesse *et al.*, 2016; Moisseev *et al.*, 2017].

567

568

569

570

571

572

To assist in interpreting the remote-sensed data, atmospheric state profiles are obtained from European Centre for Medium-Range Weather Forecasts (ECMWF) re-analysis at 1 hour temporal resolution over the site. Variables are re-interpolated onto a height grid using pressure measurements from 6 hourly radiosondes. Profiles of atmospheric temperature, pressure and humidity are used in the target classification scheme and within the retrieval algorithm to estimate radar attenuation due to atmospheric gases.

573

574

575

576

577

Prior to the retrieval remote-sensed and atmospheric data are averaged onto a common grid using the reflectivity-weighted mean Doppler velocity for averaging. A detection mask is generated for each radar instrument, using the texture of the mean Doppler velocity [Helmus and Collis, 2016] and radar signal-to-noise ratio after subtracting an estimate of the noise.

578

3.2 In situ measurements

579

580

The BAECC 2014 campaign provides a valuable opportunity to evaluate remote-sensed estimates of snow against reliable and sustained in situ observations at the surface; this is

581 rarely possible at lower latitudes where both in situ and millimeter-wavelength radar mea-
582 surements are affected by melting. Images of ice particles from the precipitation imaging
583 package (PIP) video disdrometer [Newman *et al.*, 2009] are converted to measurements of
584 particle number concentration, size, area and fallspeed. The mass of each particle is esti-
585 mated from PIP observations of particle size, area and terminal velocity as described in *von*
586 *Lerber et al.* [2017]; the maximum dimension of the ice particles are scaled to derive the par-
587 ticle masses that result in the best fit with snow accumulation measured by nearby Pluvio
588 snow gauges. PIP measurements at 5 min resolution are used, and shifted by 5 minutes for
589 comparison against remote-sensing measurements around 500 m above ground level. *Kneifel*
590 *et al.* [2015] discuss a more precise approach to estimating the time-lag for evaluation against
591 the lowest radar gates, but given the time-averaging used in this retrieval a constant lag was
592 sufficient.

593 The median diameter D_0 and normalized number concentration N_w parameters are
594 derived from the measured particle size distribution. Ice particle bulk density is estimated
595 from PIP measurements using the measured PSD and velocity-size relation, and estimated
596 mass-size relation according to (4) [*von Lerber et al.*, 2017]. This method was found to be
597 consistent with complementary methods using the Pluvio snow accumulation to estimate the
598 bulk density of ice [*Tiira et al.*, 2016; *Moisseev et al.*, 2017].

599 **4 Results**

600 We first demonstrate the retrieval for a case study (Sec. 4.1), before presenting statisti-
601 cal evaluation of retrievals over 10 snow events during the SNEX IOP (Sec. 4.2).

602 **4.1 Case study: February 21–22 2014**

603 At 23:00 UTC on February 21 2014 a warm occluded front passed over Hyytiälä,
604 bringing about an hour of snow dominated by large aggregates. The light pre- and post-
605 frontal snow was characterised by rimed particles, including both heavily rimed aggregates
606 and graupel. With a total melted-equivalent accumulation of 5 mm comprising rimed and
607 unrimed snow, this event has been extensively studied with in situ [*Tiira et al.*, 2016; *von*
608 *Lerber et al.*, 2017; *Moisseev et al.*, 2017] and radar remote-sensing [*Kneifel et al.*, 2015;
609 *Kalesse et al.*, 2016] methods. The remote-sensed and in situ measurements for this case are

610 shown in Figs. 6 and 7, respectively. We divide the case into pre-frontal, frontal and post-
611 frontal regimes.

612 In the prefrontal regime (18:00 to 23:00 UTC) snowfall is relatively constant with
613 melted-equivalent rates between 0.2 and 1 mm h⁻¹ (Fig. 7d) from clouds with tops around
614 5 km and -20 °C (Fig. 6a–c). Particles measured in situ are dominated by a high concen-
615 tration of compact ice particles, with bulk densities between 200–400 kg m⁻³. PIP imagery
616 confirms the presence of graupel during this period [Fig. 14 from *Kneifel et al.*, 2015]. In
617 the hour prior to the front, cloud-top lowers to around 3 km and -15 °C, and relatively little
618 snow is measured at the surface. *Moisseev et al.* [2017] and *von Lerber et al.* [2017] note that
619 the low particle counts measured by PIP during this period lead to reduced confidence in the
620 retrieved quantities, and the bulk density (Fig. 7d) is not retrieved here.

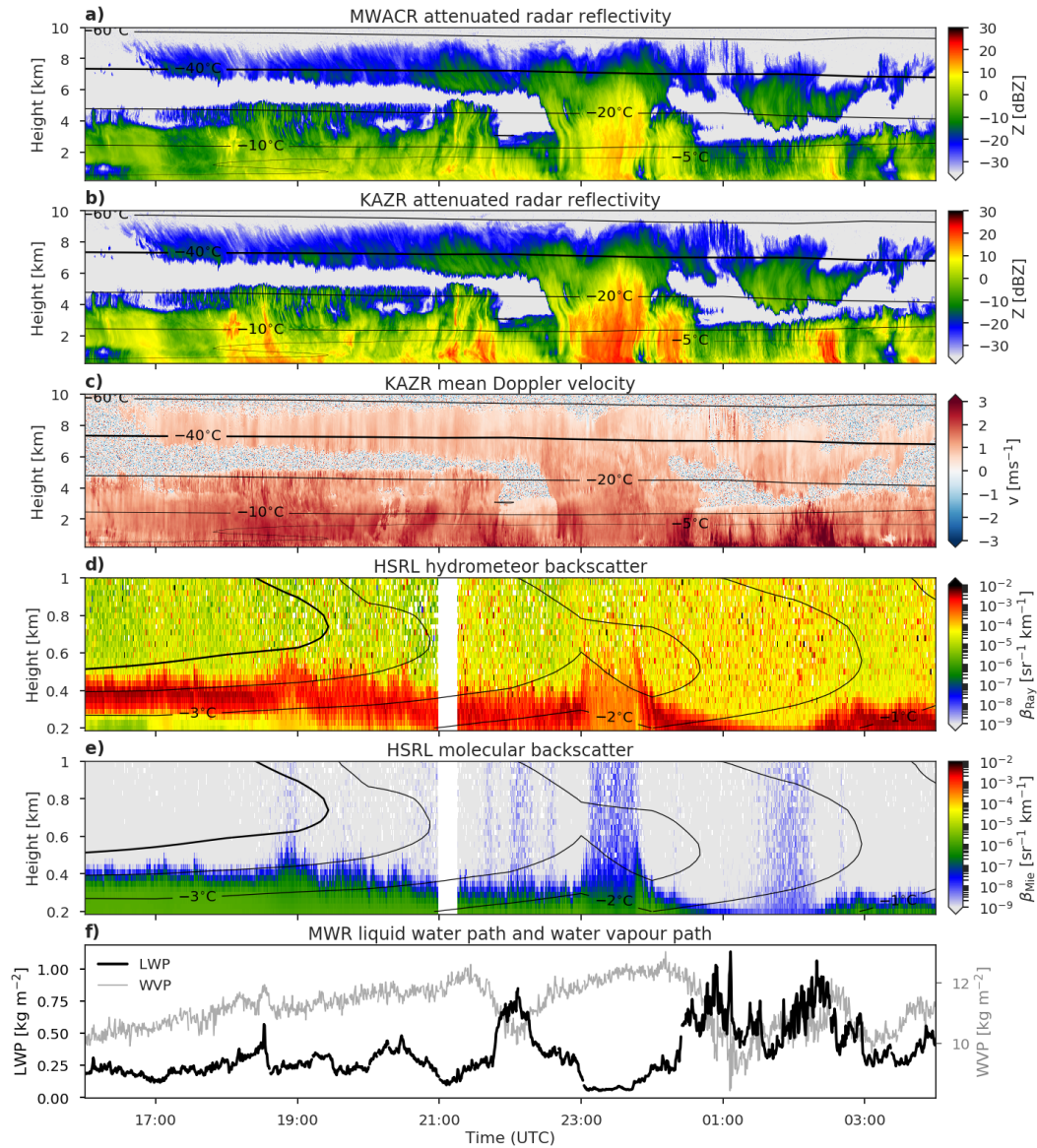
621 The frontal regime (23:00 and 00:00 UTC) brings heavier snow with a peak snowfall
622 rate of 4.0 mm h⁻¹, and PIP imagery and measurements indicate large aggregates with me-
623 dian diameters up to 5 mm (Fig. 7d); however, particle fallspeeds do not exceed 1.5 m s⁻¹
624 (Fig. 7b). Here cloud-top is around 9 km and the maximum KAZR reflectivity factor exceeds
625 20 dBZ near the surface.

626 The post-frontal regime (00:00 to 03:00 UTC) is dominated by patchy and very light
627 snow with the exception of two showers in which the snow rate exceeds 2 mm h⁻¹; cloud-
628 top is again between 3 and 5 km. PIP measurements of bulk density are higher than in the
629 pre-frontal period, between 200 and 500 kg m⁻³, and the particle size distribution confirms
630 that the post-frontal snow features a higher concentration of larger and fast-falling particles,
631 which *von Lerber et al.* [2017] noted comprised a mixture of rimed aggregates and graupel.

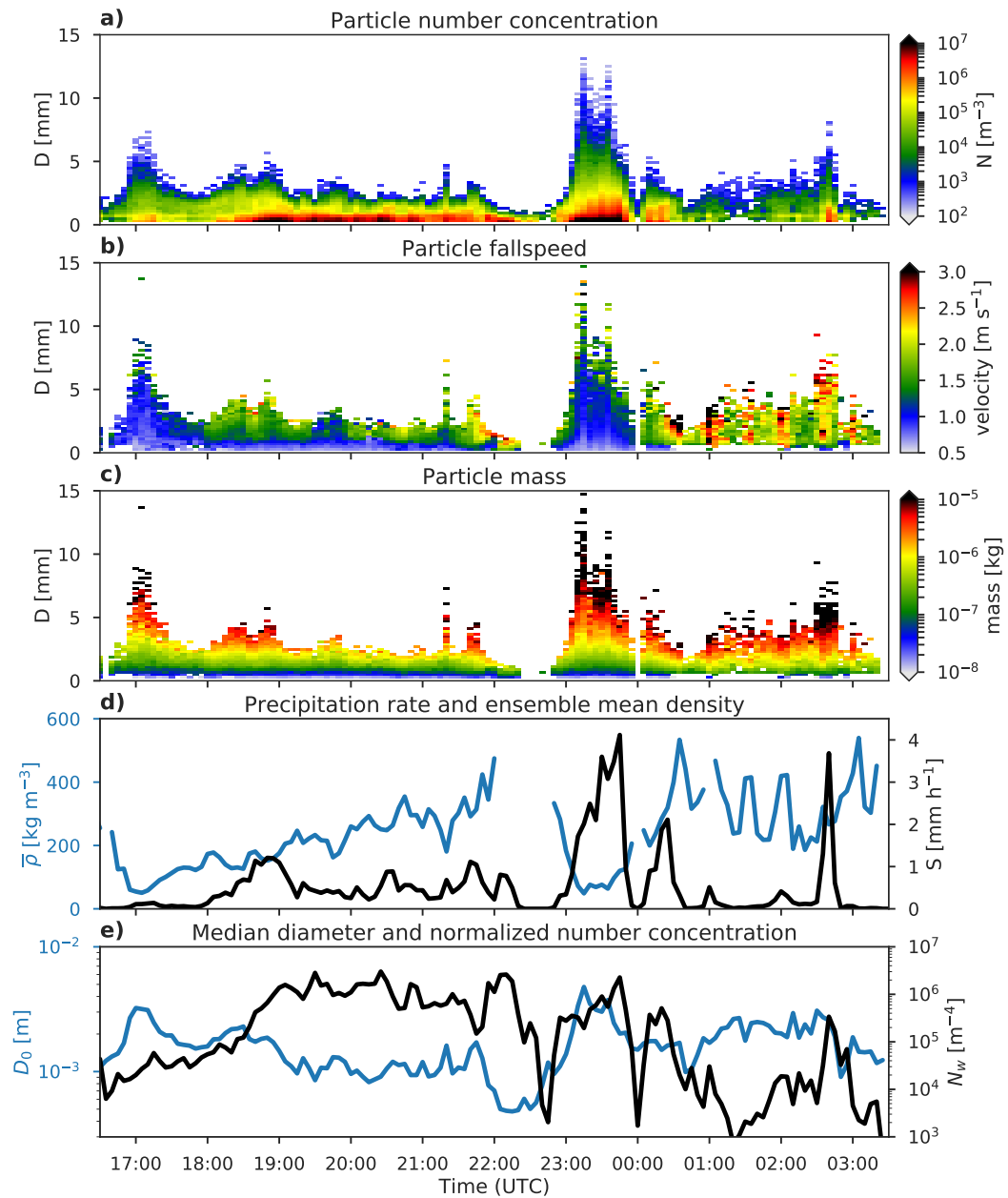
632 The presence of rimed snow and graupel throughout the pre- and post-frontal regimes
633 is indicative of persistent mixed-phase cloud layers in the lower atmosphere; however, the
634 vertical distribution of supercooled liquid water cannot be observed directly. The liquid wa-
635 ter path retrieved from microwave radiometer (Fig. 6f) and strong HSRL backscatter (Fig. 6d)
636 in the lowest liquid layers suggest that the vertically-integrated amount of liquid water in-
637 creases throughout the case, while the cloud base lowers. Above this lowest layer, *Kalesse*
638 *et al.* [2016] used Doppler spectra and soundings to infer the presence of embedded mixed-
639 phase cloud layers around 1 and 3.2 km. The exception is in the frontal snow, when both mi-
640 crowave radiometer and lidar backscatter indicate that the liquid water layers are depleted
641 [*Moisseev et al.*, 2017]. Visual inspection of the mean Doppler velocity (Fig. 6c) hints at the

signature of mixed-phase cloud layers in the reflectivity-weighted average fallspeed of snow particles: the largest near-surface mean Doppler velocities correspond in time to maxima in LWP around 22:00, 01:00 and 02:20 UTC (Fig. 6f) during the pre- and post-frontal regimes, while the frontal regime represents a minimum in both mean Doppler velocity and LWP despite being the period during which the greatest snow rate and particle size are measured. Through the vertical profile, increases in the mean Doppler velocity are evident at or around 1 and 3 km, which may be related to the onset of riming in mixed-phase cloud layers. A more quantitative estimate of riming will be made using the CAPTIVATE retrieval algorithm.

The CAPTIVATE retrieval is applied to the February 21 case, assimilating 35- and 94-GHz radar reflectivities and 35-GHZ mean Doppler velocity (hereafter “ZZV”). Recall that the 94-GHz Doppler velocity is not used due to a mispointing error. The retrieved state variables are the extinction coefficient, primed number concentration and density index (hereafter “ $\alpha_v N'_0 r$ ”). As a check on the quality of the retrieval, we confirm that the best estimate of the state can be used to forward-model the observed MWACR radar reflectivity (Fig. 8a&b) and KAZR mean Doppler velocity (Fig. 8c&d). Rather than report the values of the state variables directly, we derive more physically meaningful parameters from the retrieval: the melted-equivalent snow rate (Fig. 8e), normalized number concentration (Fig. 8f), median diameter (Fig. 8g), and the density factor (Fig. 8h). In the prefrontal regime snow rate reaches 0.1–1.0 mm h⁻¹ below 3 km. In the frontal regime the snow rate exceeds 1 mm h⁻¹ between 5–7 km above ground level; toward the surface, number concentration decreases while median diameter increases, suggesting growth by aggregation. In the post-frontal showers maxima in snow rate correspond to streaks of increased number concentration and median diameter. Of primary interest is the retrieval of the density factor, which increases to around $r = 0.2$ below 3 km in the pre-frontal and post-frontal regimes and up to local maxima of 0.5 to 0.7 near the surface around 22:00, 01:00 and 02:20 UTC; in short, the retrieved density factor maps closely to the regions of high mean Doppler velocity identified earlier. In the pre-frontal regime small but non-zero density factors are retrieved in both the cirrus and the midlevel cloud-tops, albeit with large estimated uncertainties (not shown); much of this cirrus occurs below temperatures at which supercooled liquid—and therefore riming—is to be expected (Fig. 6a–c), an occurrence which has not been excluded within the retrieval. As discussed in Section 2.2.2, small non-zero density factors are within the observed variability of mass-size relations for unrimed particles; however it may also be the case that vertical air motion dominates the mean Doppler velocity in this regions.



650 **Figure 6.** AMF2 measurements from Hyttiälä between 2014-02-21 16:00 UTC and 2014-02-22 03:00
 651 UTC. KAZR radar reflectivity (a) and mean Doppler velocity (b); MWACR radar reflectivity (c); HSRL atten-
 652 uated Mie backscatter (d) and attenuated Rayleigh backscatter (e); and microwave radiometer LWP (f). Note
 653 the different vertical scales for HSRL backscatter (d & e). Black contours are temperature from ECMWF
 654 re-analysis; a darker line at -40°C denotes the temperature below which supercooled liquid water is not
 655 expected.



656 **Figure 7.** In situ PIP measurements from Hyytiälä between 2014-02-21 16:00 UTC and 2014-02-22 05:00
 657 UTC. Particle size and fallspeed are measured, while particle mass, snow rate and bulk density are estimated
 658 as described in von Lerber *et al.* [2017].

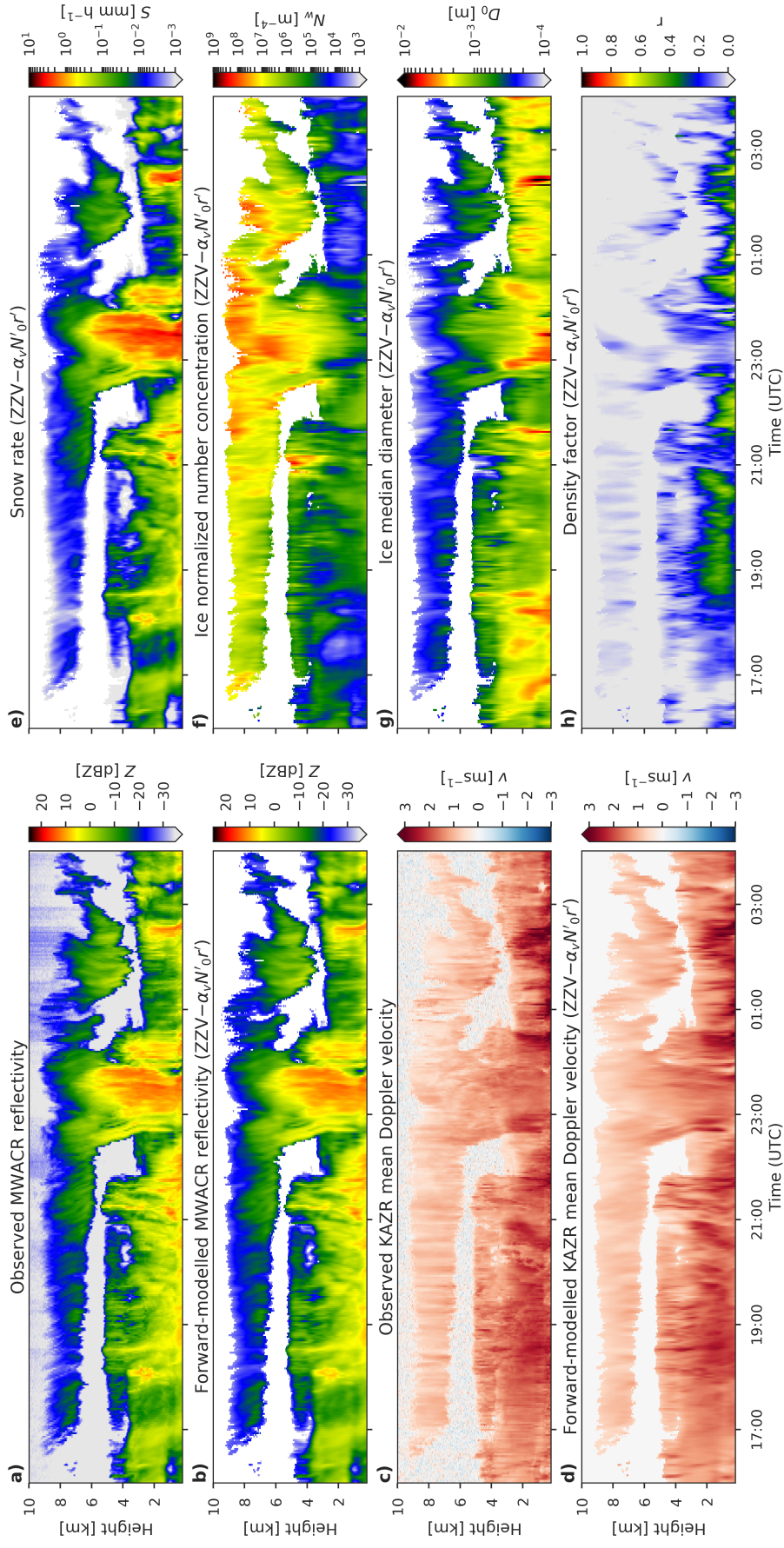
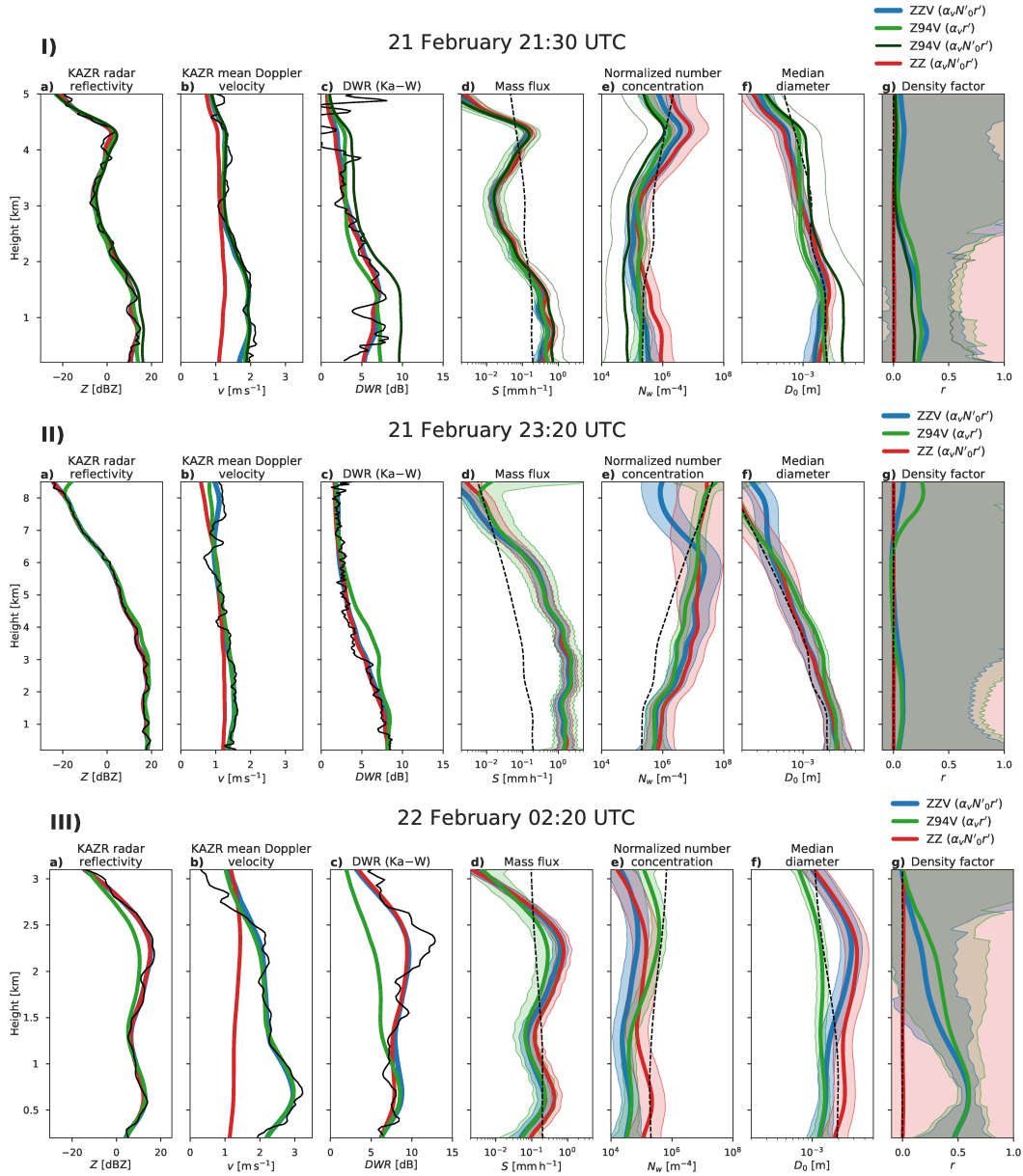


Figure 8. The observed and forward-modelled MWACR reflectivity (a & b), and observed and forward-modelled KAZR mean Doppler velocity (c & d); and the retrieved snow rate (e), normalized number concentration (f), median particle diameter (g) and density factor (h) from the ZZY retrieval for the 21 February 2014 case.

4.1.1 Profiles

In addition to assimilating all available radar measurements and retrieving all state variables, it is of interest to explore the relative contributions of Doppler and dual-frequency measurements to the CAPTIVATE retrieval. These configurations are more easily compared at selected profiles, each representing 120 S of averaged radar measurements. We select a profile from each of the snow regimes: a pre-frontal profile at 21:30 UTC (Fig. 9 I), a frontal profile at 23:20 UTC (Fig. 9 II), and a post-frontal profile at 02:20 UTC (Fig. 9 III).

The $ZZV-\alpha_v N'_0 r'$ retrieval of the pre-frontal profile (Fig. 9 I) shows snow rate increasing below 3 km to approximately 0.5 mm h^{-1} at the surface, concurrent with an increase in the density factor to around $r = 0.3$ below 1 km. Large uncertainties in the retrieved density factor reflect a large observational uncertainty of 1 m s^{-1} in the Doppler velocity; however, we find that the retrieved density factor is robust to changes in the observational uncertainty. When Doppler velocity is not assimilated ($ZZ-\alpha_v N'_0 r'$) there is little constraint on the density factor, which remains close to $r = 0$. This leads to an underestimate in forward-modelled mean Doppler velocity of as much as 1 m s^{-1} below 2 km, and N_w greater by a factor of 5 than that of $ZZV-\alpha_v N'_0 r'$; that is, when dense rimed particles are not retrieved, the lower density of ice is compensated by a larger concentration of snow particles such that the snow rate differs only slightly from that of $ZZV-\alpha_v N'_0 r'$. The $ZZ-\alpha_v N'_0 r'$ retrieval is very similar to one in which Doppler velocity is available, but where all snow is assumed to be unrimed aggregates ($ZZV-\alpha_v N'_0$; not shown). Conversely, when only MWACR reflectivities are assimilated and the full state vector is retrieved ($Z94V-\alpha_v N'_0 r'$; the dark green line in Fig. 9 I), the PSD diverges significantly from $ZZV-\alpha_v N'_0 r'$. A much lower number concentration of larger particles is retrieved, with median diameter a factor of two larger than that of $ZZV-\alpha_v N'_0 r'$. Despite a lower density factor, this retrieval appears well-constrained by the Doppler velocity—but the forward-modelled DWR indicates that the larger particles lead to an error in Ka-band reflectivity of around 4 dB near the surface. This is an example of an under-constrained retrieval in which three state variables are estimated from two measured variables. A better-posed retrieval can be made by treating the primed number concentration as a model variable which does not vary from the prior $Z94V-\alpha_v r'$ (the bright green line in Fig. 9). The results of this retrieval much more closely resemble $ZZV-\alpha_v N'_0 r'$, with reduced errors in forward-modelled DWR and values of N'_0 and D_0 closer to their priors; therefore in subsequent profiles only the $Z94V-\alpha_v r'$ will be compared with $ZZV-\alpha_v N'_0 r'$ and $ZZ-\alpha_v N'_0 r'$.



691 **Figure 9.** Forward-modelled measured variables and retrieved snow rate, normalized number concentra-
 692 tion, median diameter and density factor for ZZV, Z94V and ZZ retrievals, for a profile at 21:30 UTC (I) ,
 693 23:20 UTC (II) and 02:20 UTC (III) within the pre-frontal regime. Black solid lines indicate the observed
 694 variables, and dashed lines indicate the prior retrieved variables. Shading indicates the 5th to 95th percentile
 695 uncertainty of the retrieval.

722 In the frontal regime (Fig. 9 II) there is generally good agreement between retrievals,
 723 which consistently represent a snow rate of 1 to 2 mm h⁻¹ below 4 km; this relatively constant
 724 mass flux corresponds with increasing median diameter and decreasing number concentra-
 725 tion consistent with strong aggregation in the shower, and confirmed by the large aggregate
 726 snowflakes observed at the surface (Fig. 7). Both ZZV and Z94V diagnose small non-zero
 727 density factors below about 4 km, without which ZZ under-estimates the mean Doppler ve-
 728 locity by around 0.5 m s⁻¹. In the mid-levels Z94V overestimates KAZR radar reflectivities,
 729 once again due to a smaller concentration of larger particles. In most other regards the re-
 730 trievals are similar until near cloud-top, where relatively large Doppler velocities lead to the
 731 retrieval of small to moderate density factors in ZZV and Z94V which are unphysical (the
 732 contours in Fig. 6 indicate that the temperature is below -40°C at these heights), and may be
 733 a result of vertical air motion in the cirrus. In stratiform precipitation, the retrieval of dense
 734 ice due to small-scale turbulent features in vertical air motion is somewhat suppressed by
 735 the use of a Kalman smoother in the retrieval of the density index; however, it would also be
 736 possible within CAPTIVATE to reduce prior uncertainty in the density factor where riming
 737 is unlikely, or to apply higher uncertainties to mean Doppler velocity measurements where
 738 larger contributions from vertical air motion are expected.

739 In the postfrontal regime (Fig. 9 III) the Doppler velocity reaches 3 m s⁻¹ below 1 km,
 740 where ZZV and Z94V estimate density factors around $r = 0.6$; ZZ does not diagnose resolve
 741 this increase in particle density, and the corresponding forward-modelled mean Doppler ve-
 742 locity differs from observations by almost 2 m s⁻¹ along with overestimates in both number
 743 concentration and median size. While ZZV and Z94V converge upon similar PSDs below
 744 1.5 km where the Doppler signal is strong, near the top of the cloud Z94V remains closer to
 745 its priors (recall that N'_0 does not vary in this retrieval), leading to a much higher concentra-
 746 tion of small particles and a significant under-estimate of the KAZR radar reflectivity above
 747 1.5 km.

748 While the uncertainties in the retrieved density factor are constrained in the parts of the
 749 profile where the mean Doppler velocity of denser particles differ significantly from that of
 750 unrimed aggregates—typically below 2 or 3 km in these profiles—very large density factor
 751 uncertainties are evident aloft. In these regions the Doppler velocity contains little informa-
 752 tion about variations in density because the smallest particles are assumed to be solid quasi-
 753 spheroidal particles for all values of the density factor (see Fig. 3).

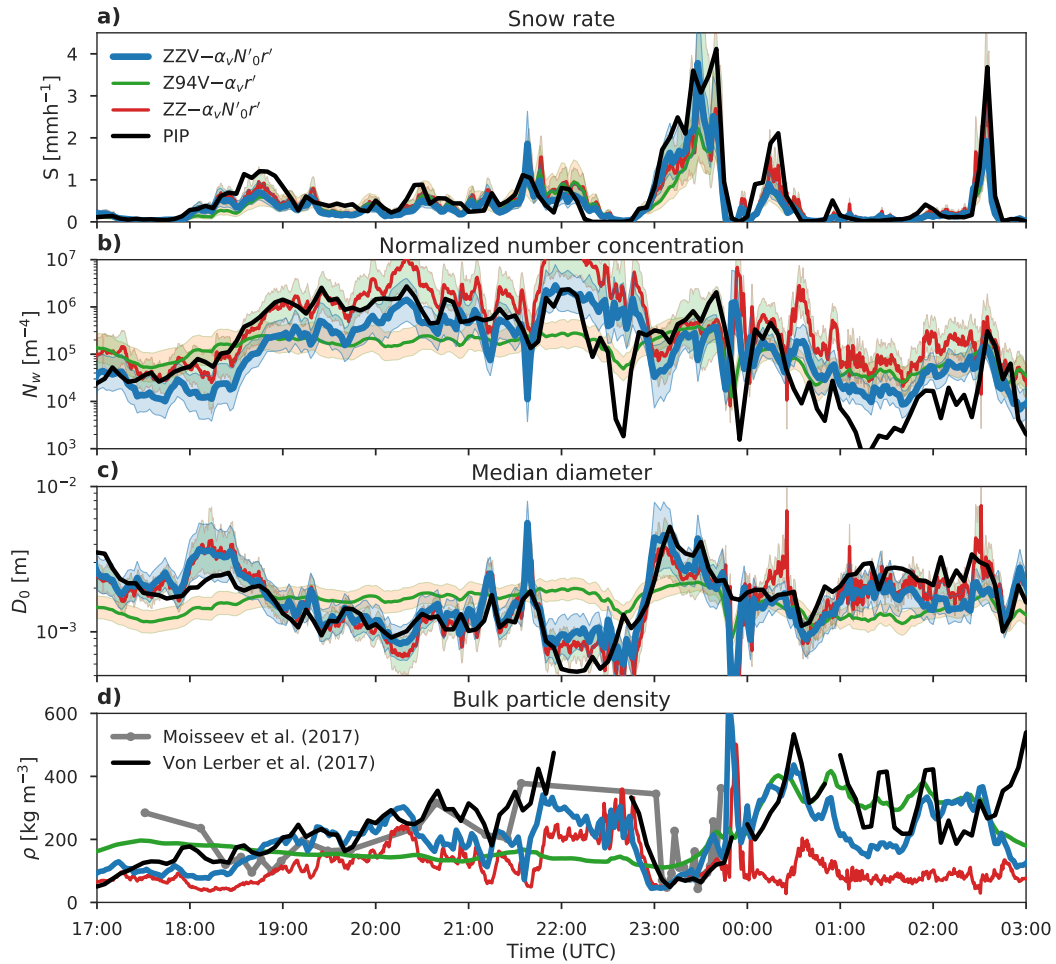
754 **4.1.2 Comparison against in situ measurements**

755 We now evaluate the CAPTIVATE retrievals against in situ measurements at the sur-
 756 face; ZZV, Z94V and ZZ estimates of snow rate, normalized number concentration, median
 757 diameter, and bulk density averaged over the radar gates up to 600 m above ground level are
 758 compared against those from PIP (Fig. 10).

759 All of the CAPTIVATE retrievals of snow rate are within the range of uncertainty of
 760 PIP snow rate, with under-estimates of up to 50 % especially evident in frontal and post-
 761 frontal showers. As was also the case in the analysis of profiles, the estimated snow rates are
 762 remarkably consistent between the different retrievals; this is despite significant differences
 763 in estimates of particle size, number concentration and density.

769 As they often compensate for one another, the parameters of the PSD are evaluated
 770 together. ZZV and ZZ estimates of median diameter (Fig 10c) are within 50 % of PIP mea-
 771 surements, and estimates of normalized number concentration (Fig 10b) are usually within
 772 the retrieval uncertainty—with errors of up to a factor of five—of PIP measurements. With-
 773 out a dual-frequency constraint on particle size and therefore fewer state variables retrieved,
 774 the Z94V- $\alpha_v r'$ estimates of N'_0 and D_0 are less able to resolve the distinct snow regimes: in
 775 the pre-frontal period Z94V number concentrations exceed PIP measurements by up to an or-
 776 der of magnitude while particle sizes may be double the surface observations; the inverse is
 777 true in the post-frontal period.

778 Finally we evaluate the retrieval against in situ measurements of bulk density (Fig. 10d).
 779 The volume flux-weighted bulk density is estimated from retrieved particle properties consis-
 780 tent with eq. 4, in which the mass- and velocity-size relations are modulated by the retrieved
 781 density factor. We compare this remote-sensed estimate against two in situ retrievals of bulk
 782 density from PIP measurements [von Lerber *et al.*, 2017] and a combination of PIP and Plu-
 783 vio snow gauge measurements [Moisseev *et al.*, 2017] to constrain the total accumulation; we
 784 note that the former method was calibrated against the latter, so these two retrievals are not
 785 independent. The retrieved density factor and median diameter are both important to the es-
 786 timated bulk density; when constrained by both Doppler and dual-frequency measurements,
 787 ZZV is therefore broadly capable of resolving the bulk density measured by PIP, although
 788 we note underestimates of 25–50 % between 20:30 and 22:00 in the pre-frontal period, and
 789 between 01:00 and 01:45 in the post-frontal period. Errors in Z94V estimates of median di-
 790 ameter can either exacerbate (in the pre-frontal regime) or mask (in the post-frontal) errors



764 **Figure 10.** Time series comparing mean retrieved variables over the lowest radar gates (between 300 m and
 765 600 m) against the in situ PIP measurements at the surface. Shaded areas indicate the 5th and 95th percentile
 766 uncertainty of the retrieval. Surface observations are shifted by 5 minutes. The bulk ice density is discontin-
 767 uous where very small median diameter leads to erroneously high densities, as discussed in *von Lerber et al.*
 768 [2017].

791 in the bulk density: as discussed above, with a weaker constraint on particle size Z94V does
 792 not resolve the compact graupel ahead of the front, and underestimates post-frontal particle
 793 size. Conversely, without Doppler information the bulk density estimates from ZZ are chiefly
 794 a function of particle size: density rarely exceeds 200 kg m^{-3} except immediately ahead of
 795 the front, when median diameters of less than 1 mm are estimated.

796 **4.1.3 Riming as an indicator of mixed-phase cloud**

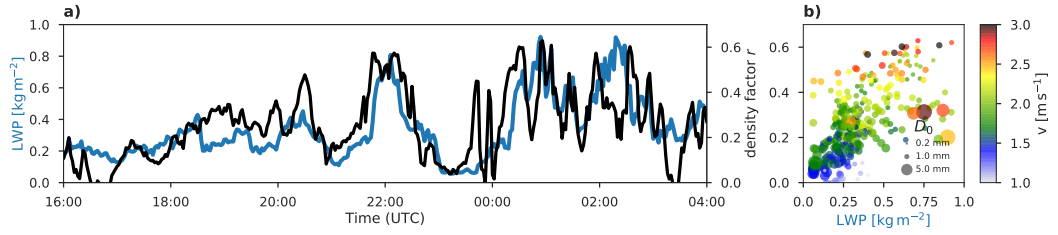
797 While CAPTIVATE has been developed for radar–lidar–radiometer synergy retrievals,
 798 in the present case the lidar is fully extinguished within less than 1 km of the surface in the
 799 lowest of several shallow layers of mixed-phase cloud. Our retrievals assimilate radar reflec-
 800 tivity and mean Doppler velocity, both of which are dominated by backscatter from larger
 801 ice particles; the Doppler spectrum or its higher moments can sometimes be used to iden-
 802 tify the presence of liquid cloud [Kalesse *et al.*, 2016], although the broader applicability of
 803 these methods can be limited, especially for retrievals from airborne and spaceborne plat-
 804 forms where spectral broadening is significant [e.g. Illingworth *et al.*, 2015]. The density of
 805 ice particles has been retrieved based on mean Doppler velocity, relying on approximations
 806 to the morphology of ice particles from unrimed aggregates to graupel and their associated
 807 terminal fallspeeds. We hypothesise that the primary process by which high density factors
 808 occur is the riming of ice particles within mixed-phase clouds. An independent source of in-
 809 formation on the potential for riming is LWP retrieved from the microwave radiometer; *von*
 810 *Lerber et al.* [2017] used LWP as a proxy for riming, and the connection between LWP and
 811 rime mass fraction is also demonstrated from in situ retrievals in *Moisseev et al.* [2017].

812 For the present case, the timeseries of LWP is strongly correlated to the CAPTIVATE
 813 retrievals of density factor in the near-surface gates (Fig. 11a; $ZZV-\alpha_v N'_0 r'$). The highest
 814 density factors correspond to the presence of significant mixed-phase cloud in the pre- and
 815 post-frontal periods, and the dominance of unrimed aggregates to the depletion of liquid ev-
 816 ident during the frontal snow. The scatter plot of the LWP versus the retrieved density factor
 817 (Fig. 11b) is coloured by the mean Doppler velocity and sized by retrieved median diameter.
 818 At low LWP particles tend to be large unrimed aggregates with mean Doppler velocities less
 819 than 2 m s^{-1} . Moderate LWP profiles correspond to particles ranging from larger rimed ag-
 820 gregates with $0.0 < r < 0.2$, to compact rimed aggregates ($0.2 < r < 0.5$). At high LWP the
 821 snow is dominated by graupel ($0.5 < r < 0.8$), with some instances of larger, fast-falling and
 822 heavily-rimed aggregates.

826 In summary, the February 21 2014 case study includes significant riming below around
827 3 km during pre- and post-frontal snow, interrupted by a frontal shower dominated by large
828 aggregate snowflakes. Mean Doppler velocity provides an effective constraint on estimates
829 of the density factor, retrieved values of which varied from $r \approx 0.1$ for unrimed aggregates
830 $r \approx 0.6$ for graupel. Dual-frequency radar reflectivity proved critical to constraining esti-
831 mates of the particle size distribution, leading to significant improvements in retrieved quan-
832 tities when compared with in situ measurements at the surface. While the single-frequency
833 retrieval was capable of similar estimates of snow rate and density factor, the retrieval was
834 better constrained when a single parameter of the PSD was retrieved, leading to estimates
835 closer to the priors in which compact pre-frontal graupel was not resolved. Our hypothesis
836 that the retrieved density factor varies chiefly due to the riming of ice particles in mixed-
837 phase cloud layers is supported by a strong association between the density factor and an
838 independent estimate of supercooled liquid water.

839 4.2 SNEX 2014 IOP

840 In this section the LWP is used as an indicator of the availability of SLW for riming,
841 hence to distinguish between unrimed and rimed snow, and heavily rimed snow or graupel.
842 Snow events during the SNEX IOP were identified by *von Lerber et al.* [2017] wherein sig-
843 nificant snow was falling at the surface and the surface temperature was below freezing (Ta-
844 ble 3). A probability density function of LWP over the SNEX IOP (Fig. 12a) illustrates that,
845 while the majority of the snow events during the period occurred in low-LWP conditions,
846 significant SLW is relatively frequent during the IOP. Following a similar distinction made
847 in *von Lerber et al.* [2017], three ranges of LWP are used to distinguish between unrimed
848 ($LWP < 0.1 \text{ kg m}^{-2}$), moderately rimed ($0.1 \leq LWP < 0.3 \text{ kg m}^{-2}$), and heavily rimed snow
849 or graupel ($LWP \geq 0.3 \text{ kg m}^{-2}$). In that study the mass-size and fallspeed-size relations from
850 in situ measurements of particles were shown to be consistent with the LWP classification.
851 Unrimed snow accounts for just over half of the profiles; rimed snow around 30 %, and grau-
852 pel around 10 %; in the rest, no significant snow was measured and the profile was skipped.
853 While the unrimed snow is associated with the coldest surface temperatures (Fig. 12b) on
854 average, all three categories are most frequent at temperatures just below freezing; it is not
855 evident that the riming events can be distinguished by temperature. Similarly, the low-LWP
856 regime includes almost all events with low relative humidities (Fig. 12c), but all categories
857 occur most frequently at relative humidities greater than around 90 %.



823 **Figure 11.** Time series (a) and scatter plot (b) of $ZZV - \alpha_v N'_0 r'$ density factor in the lowest radar gates
 824 (300m to 600m) against LWP measured by the microwave radiometer. In the scatter plot the markers are
 825 coloured by the mean Doppler velocity, and sized according to the retrieved median diameter.

858

Table 3. Snow events during SNEX 2014 IOP

Date (UTC) 2014	Melted-equivalent accumulation [mm]	Surface temperature (°C)	
		Min	Max
*1 Feb 00:00—06:00	7.4	−9.8	−8.9
*1 Feb 10:00—16:00	1.4	−7.9	−7.0
2 Feb 16:00—19:00	1.7	−5.4	−5.2
12 Feb 04:00—09:00	0.8	−1.0	0.0
15 Feb 21:00—16 Feb 02:00	2.6	−2.1	−1.0
21 Feb 16:00—22 Feb 03:30	5.0	−2.7	0.0
15 Mar 05:00—07:00	0.3	−2.0	−1.3
*18 Mar 08:00—19:00	4.4	−3.8	−1.8
19 Mar 00:00—20:00	1.5	−7.3	−3.7
20 Mar 16:00—00:00	6.1	−4.3	−1.3

* Denotes events where dual-frequency radar data were not always available.

861 The CAPTIVATE best estimate ($ZZV-\alpha_v N'_0 r'$) was run over approximately 55 hours
 862 of available dual-frequency Doppler radar data. Joint histograms of the profile of forward-
 863 modelled observed variables and retrieved variables are shown for each of the LWP classifi-
 864 cations (Fig. 13).

865 The unrimed snow (Fig. 13-I; $LWP < 0.1 \text{ kg m}^{-3}$) is associated with the lowest mean
 866 Doppler velocities (Fig. 13-Ib), which average around 1 m s^{-1} near the surface and never ex-
 867 ceed 2 m s^{-1} . The corresponding median density factor (Fig. 13-Ig) is between 0 and 0.2
 868 below 4 km; this is consistent with the finding of *Moisseev et al.* [2017] that the mass-size of
 869 unrimed aggregate snow at Hyytiälä is consistently higher than that of *Brown and Francis*
 870 [1995], corresponding to roughly $r = 0.15$ in Fig. 1. In the earlier profile of unrimed snow
 871 (Fig. 9 II) it was noted that ice water content remained constant with height near the surface
 872 while diameter increased and number concentration decreased; these characteristic features
 873 of aggregation are robustly present in approximately 30 hours of aggregate snowfall, with
 874 the median snow rate (Fig. 13-Id) constant below 3 km, concurrent with an increase in me-
 875 dian size (Fig. 13-If) and a decrease in number concentration (Fig. 13-Ie) toward the surface.
 876 The gradient in D_0 represents roughly a doubling in median particle diameter over 2 km. The
 877 Ka-W dual-wavelength ratio increases below 3 or 4 km to a median of around 5 dB; how-
 878 ever, comparison to the triple-frequency data (Fig. 5) shows that values in this range are not
 879 unique to either aggregates or graupel; a third radar frequency would provide valuable infor-
 880 mation to help constrain a retrieval based on the different scattering signatures of unrimed
 881 aggregates and heavily rimed particles.

882 In the rimed snow (Fig. 13 II; $0.1 \leq LWP < 0.3 \text{ kg m}^{-3}$) mean Doppler velocities
 883 (Fig. 13IIb) are between 1 and 2 m s^{-1} near the surface, corresponding to density factors
 884 that increase below about 4 km to between 0 and 0.4 in the lowest 2 km. Unlike the unrimed
 885 snow, the snow rate (Fig. 13 IIId) continues to increase toward the surface, indicating an ad-
 886 dition of ice water content which may be due to accretion of supercooled liquid or vapour
 887 deposition. The near-surface gradients of N'_0 and D_0 (Fig. 13 IIe & f) are not significantly
 888 reduced from those in unrimed snow, so it seems likely that a mix of aggregation, riming and
 889 deposition processes occur within this regime.

890 Finally, the heavily rimed snow or graupel (Fig. 13 III; $LWP \geq 0.3 \text{ kg m}^{-3}$) is associ-
 891 ated with mean Doppler velocities (Fig. 13 IIIb) up to 3 m s^{-1} and density factors (Fig. 13
 892 IIIg) increasing steeply below 3 km up to as much as $r = 0.5$ with a median around $r = 0.3$.

893 Unlike the unrimed and rimed snow regimes, the snow rate in this regime increases rapidly
894 toward the surface, with the median snow rate increasing by an order of magnitude over the
895 lowest 2 to 3 km—a rate similar to that in the upper-level clouds of all regimes—however,
896 D_0 and N'_0 are near-constant in the lower levels. This is consistent with an accretion of mass
897 due to riming, although deposition cannot be ruled out. An increase in normalized number
898 concentration may be discernible near the surface (Fig. 13 IIIg), perhaps suggesting a relative
899 increase in the concentration of small particles, or a breakup of larger particles. This may
900 be indicative of a secondary ice generation process such as rime splintering; however, more
901 work would be required to confirm this, and to what degree the present retrieval may help in
902 the study of secondary ice processes.

903 An evaluation of the CAPTIVATE retrieval over all available dual-frequency Doppler
904 radar data from the SNEX IOP has shown characteristic differences between the profiles of
905 snow rate, PSD parameters and density factor between profiles of unrimed and rimed snow.
906 LWP provides a suitable proxy to distinguish between unrimed and heavily rimed snow
907 events. This initial analysis has focused on demonstrating the potential to resolve key micro-
908 physical processes from the Doppler velocity; however, many other analyses of the meteorological
909 and thermodynamical context of riming and aggregation processes may be envisaged.

910 **5 Discussion and conclusions**

911 The morphology of an ice particle is a record of the microphysical processes by which
912 it forms; in this study we have proposed a simple parameterisation for the representation of
913 the wide range of ice particle densities and shapes from unrimed aggregate snowflakes to
914 graupel and hail. Remote-sensed estimates of snow typically assume snow particles that re-
915 semble unrimed aggregates; however, riming is both a critical process for surface hydrology
916 and a control on radiatively-important mixed-phase clouds which are difficult to remote-
917 sense and poorly represented in numerical models. We have demonstrated a method for di-
918 agnosing riming within the framework of CAPTIVATE, an optimal estimation algorithm for
919 radar–lidar–radiometer retrievals of clouds, aerosols and precipitation.

920 The retrieved density factor modulates the density, shape and radar scattering cross-
921 section of ice particles, and is chiefly inferred from mean Doppler velocity, a measure of
922 reflectivity-weighted particle terminal velocities. Many refinements to this parameterisa-
923 tion may be envisaged to better represent the microphysical processes in question, and the

924 sensitivity of the retrieval to the formulation of the density factor and its effect on the mass,
925 area and scattering cross-sections of ice particles requires further study. An alternative pa-
926 rameterisation intended to more closely resemble the conceptual model for the riming of
927 aggregate snowflakes was tested using a reference mass-size relation for unrimed aggregates
928 at Hyytiälä [von Lerber *et al.*, 2017] with a constant exponent of $b_m = 2.1$, and where only
929 the prefactor of the mass-size relation was scaled with the density factor. This representa-
930 tion is more consistent with the conceptual model of the “in-filling” stage of riming, but does
931 not encompass the observed variability amongst unrimed snowflakes or the higher exponents
932 of heavily rimed graupel-like particles. The retrieved snow rate and PSD were not strongly
933 sensitive to changes in how particle density is allowed to vary, suggesting the two parame-
934 terisations allow for similar representation of unrimed to lightly rimed aggregates despite
935 some change in the mass-size exponent; however, in situ measurements of snow rate and bulk
936 particle density agreed better with the original retrieval in the densest post-frontal snow, sug-
937 gesting the advantages of representing a broader range of particle morphologies, especially
938 of heavily rimed graupel-like particles. Our prior density factor of $r = 0$ relates to the un-
939 rimed aggregates of *Brown and Francis* [1995], but it may be possible to implement more
940 sophisticated priors or constraints on the retrieval based on the atmospheric state [e.g. *Lin*
941 *and Colle*, 2011; *Szyrmer and Zawadzki*, 2014], or from regional climatologies, to better
942 resolve this variability; for example, *Moisseev et al.* [2017] showed that the lowest-density
943 particles at Hyytiälä were significantly more dense than those of *Brown and Francis* [1995],
944 and this could be represented with an updated prior of $r \approx 0.15$ near the surface. Concurrent
945 remote-sensed and in situ measurements from the BAECC 2014 campaign have provided an
946 invaluable opportunity to evaluate retrievals of rimed snow. Sustained particle imaging and
947 multiple-frequency radar measurements from Hyytiälä and other ARM and CloudNet “super-
948 sites” will provide critical datasets for the improved representation of snow microphysics, as
949 well as validation for future satellite retrievals.

950 The CAPTIVATE retrieval was applied to vertically-pointing Ka- and W-band Doppler
951 radar measurements from 10 snow events over the SNEX IOP of BAECC 2014. Dual-frequency
952 and Doppler radar measurements provided sufficient information to retrieve two parameters
953 of the PSD as well as the density factor. The dual-frequency radar reflectivities and mean
954 Doppler velocity make distinct contributions to the retrieval, with radar reflectivities at Ka-
955 and W bands providing a strong constraint on the particle size distribution but relatively little
956 information on density; Doppler velocity provided the sole constraint on the density factor.

957 Estimates of near-surface snow rate were within 50 % of in situ measurements both with and
958 without Doppler and dual-frequency measurements, showing a remarkably robust retrieval of
959 ice water content from 94-GHz radar reflectivity; however, to accurately estimate the param-
960 eters of the PSD as well as the bulk ice density, it was important to have both dual-frequency
961 and Doppler information. With the recent availability of multiple-frequency Doppler radar
962 observations of snow, and supported by observational and theoretical insights into the triple-
963 frequency signatures of rimed and unrimed ice [e.g. *Kneifel et al.*, 2018], it will become in-
964 creasingly important to quantify the information content of each additional observational
965 variable within an optimal estimation framework.

966 The retrieval of riming provides an indirect insight into the presence of supercooled
967 liquid water, and it may hence be possible to use spaceborne Doppler radars to better quan-
968 tify the frequency and distribution of embedded mixed-phase clouds—at least where pre-
969 cipitating ice is present. Using LWP as a proxy for riming provided a robust distinction be-
970 tween retrieved snow profiles of unrimed aggregates, rimed aggregates and graupel; no such
971 clear distinction was evident in surface temperature or relative humidity. For profiles with
972 low LWP the dominant growth process near the surface was aggregation, while in high-LWP
973 conditions the accretion of ice mass due to riming was evident. The ability to distinguish be-
974 tween microphysical processes through the profile suggests the potential for using multiple-
975 frequency and Doppler radars to estimate rime mass content and relate it to the budget of
976 supercooled liquid [e.g. *Moisseev et al.*, 2017], as well as to estimate microphysical process
977 rates [e.g. *Mace and Benson*, 2017]. These features were best resolved in retrievals com-
978 bining dual-frequency and Doppler measurements; however, the onset of riming was also
979 reliably detected with single-frequency radar retrievals, which could be sufficient to provide
980 improved insights into the position of embedded mixed-phase layers within optically thick
981 ice clouds from space.

982 In the mixed-phase cloud situations in which riming occurs, ground-based lidars are
983 quickly attenuated by liquid water near the surface. Therefore it was not possible in this
984 study to exploit radar–lidar synergy, either for the retrieval of ice [e.g. *Delanoë and Hogan*,
985 2010] or for a simultaneous estimate of ice and liquid; instead a correction for liquid atten-
986 uation was applied to the radar reflectivity, and the retrieval carried out only for ice. LWP
987 estimates from a co-located microwave radiometer were combined with an assumption about
988 the vertical distribution of liquid water to estimate the radar attenuation as a pre-processing
989 step before the radar retrieval. A more satisfactory approach within the optimal estimation

990 retrieval framework would be to include a microwave radiometer forward model and perform
991 a synergy retrieval, building upon studies into the active and passive microwave scattering
992 of snow [e.g. *Kneifel et al.*, 2010]. This would provide additional constraints on retrievals of
993 cloud and precipitation to those provided by other passive shortwave and longwave radiances
994 [e.g. *Leinonen et al.*, 2016] or path-integrated attenuation from surface radar backscatter [e.g.
995 *Haynes et al.*, 2009; *Hawkness-Smith*, 2010].

996 The CAPTIVATE retrieval has been developed for the synergy of EarthCARE’s 94-
997 GHz cloud profiling Doppler radar [*Illingworth et al.*, 2015] with high-spectral resolution at-
998 mospheric lidar and multi-spectral imaging radiometer. The capabilities of multiple-frequency
999 Doppler radars—as well as synergies with a range of active and passive measurements in-
1000 cluding microwave radiometers—are also of interest. In this study we have considered the
1001 contribution of Doppler velocity and dual-frequency radars to the optimal estimation of
1002 snow, following a previous study using airborne dual-frequency Doppler radars for CAP-
1003 TIVATE retrievals of tropical rain [*Mason et al.*, 2017]. Retrievals assimilating both dual-
1004 frequency and Doppler radar measurements to retrieve two parameters of the ice PSD and
1005 the density factor performed best, producing estimates of particle number concentration,
1006 size and bulk density near the surface that were close to in situ measurements. A single-
1007 frequency Doppler radar was best constrained when retrieving a single parameter of the
1008 PSD; however, we demonstrated that such a retrieval was sufficient to diagnose rimed snow
1009 in stratiform snow—wherein the mean Doppler velocity can be assumed to be dominated by
1010 hydrometeor fallspeed and not vertical air motion—and that the retrieval is robust to large
1011 observational uncertainties. The many challenges of making use of Doppler velocity mea-
1012 surements from space—including vertical resolution, horizontal averaging [e.g. *Kollias et al.*,
1013 2014], ground clutter, and radar mispointing [e.g. *Battaglia and Kollias*, 2015]—have not
1014 been considered here, and work is ongoing to apply radar simulators to airborne and ground-
1015 based measurements or numerical models to better understand the outlook for retrievals
1016 from EarthCARE [e.g. *Battaglia and Tanelli*, 2011]. Beyond EarthCARE, the prospect of
1017 spaceborne multiple-frequency Doppler radars [*National Academies of Sciences Engineering
1018 and Medicine*, 2018] provides opportunities for further advancements in the global remote-
1019 sensing of ice, including estimates of the morphology and microphysics of snow and insights
1020 into mixed-phase clouds.

1021 **Acknowledgments**

1022 We thank three anonymous reviewers for motivating significant improvements to this study,
 1023 and Chris Westbrook for helpful discussions throughout. Alessio Bozzo is thanked for his
 1024 contribution to the development of the CAPTIVATE software. This work is supported by the
 1025 National Centre for Earth Observation (NCEO) and European Space Agency Grant 4000112030/15/NL/CT,
 1026 with computing resources provided by the University of Reading. C. Chiu is funded by the
 1027 Office of Science (BER), DOE under grant DE-SC0011666. D. Moisseev acknowledges
 1028 the funding received by ERA-PLANET, trans-national project iCUPE (Grant Agreement
 1029 no. 689443), funded under the EU Horizon 2020 Framework Programme and Academy of
 1030 Finland (grants 307331 and 305175). Contributions by S. Kneifel were carried out within the
 1031 Emmy-Noether Group OPTIMIce funded by the German Science Foundation (DFG) under
 1032 Grant KN 1112/2-1.

1033 BAECC 2014 radar data are available from the ARM data archive (www.arm.gov/data),
 1034 and PIP particle measurements for two years at Hyytiälä can be accessed at github
 1035 (github.com/dmoisseev/Snow-Retrievals-2014-2015).

1036 **References**

- 1037 Battaglia, A., and P. Kollias (2015), Using Ice Clouds for Mitigating the EarthCARE
 1038 Doppler Radar Mispointing, *IEEE Transactions on Geoscience and Remote Sensing*,
 1039 *53*(4), 2079–2085, doi:10.1109/TGRS.2014.2353219.
- 1040 Battaglia, A., and S. Tanelli (2011), DOMUS: DOPpler MULTiple-Scattering Simula-
 1041 tor, *IEEE Transactions on Geoscience and Remote Sensing*, *49*(1), 442–450, doi:
 1042 10.1109/TGRS.2010.2052818.
- 1043 Brown, P. R. A., and P. N. Francis (1995), Improved Measurements of the Ice Water Content
 1044 in Cirrus Using a Total-Water Probe, *Journal of Atmospheric and Oceanic Technology*,
 1045 *12*(2), 410–414, doi:10.1175/1520-0426(1995)012<0410:IMOTIW>2.0.CO;2.
- 1046 Cadeddu, M. P., J. C. Liljegren, and D. D. Turner (2013), The Atmospheric radiation mea-
 1047 surement (ARM) program network of microwave radiometers: instrumentation, data, and
 1048 retrievals, *Atmospheric Measurement Techniques*, *6*(9), 2359–2372, doi:10.5194/amt-6-
 1049 2359-2013.
- 1050 Casella, D., G. Panegrossi, P. Sanò, A. C. Marra, S. Dietrich, B. T. Johnson, and
 1051 M. S. Kulie (2017), Evaluation of the GPM-DPR snowfall detection capabil-
 1052 ity: Comparison with CloudSat-CPR, *Atmospheric Research*, *197*, 64–75, doi:

- 1053 10.1016/J.ATMOSRES.2017.06.018.
- 1054 Ceccaldi, M., J. Delanoë, R. J. Hogan, N. L. Ponder, A. Protat, and J. Pelon (2013), From
1055 CloudSat-CALIPSO to EarthCare: Evolution of the DARDAR cloud classification and
1056 its comparison to airborne radar-lidar observations, *Journal of Geophysical Research:
1057 Atmospheres*, 118(14), 7962–7981, doi:10.1002/jgrd.50579.
- 1058 Cesana, G., J. E. Kay, H. Chepfer, J. M. English, and G. de Boer (2012), Ubiquitous
1059 low-level liquid-containing Arctic clouds: New observations and climate model
1060 constraints from CALIPSO-GOCCP, *Geophysical Research Letters*, 39(20), doi:
1061 10.1029/2012GL053385.
- 1062 Chen, S., Y. Hong, M. Kulie, A. Behrangi, P. M. Stepanian, Q. Cao, Y. You, J. Zhang, J. Hu,
1063 and X. Zhang (2016), Comparison of snowfall estimates from the NASA CloudSat Cloud
1064 Profiling Radar and NOAA/NSSL Multi-Radar Multi-Sensor System, *Journal of Hydrol-
1065 ogy*, 541, 862–872, doi:10.1016/j.jhydrol.2016.07.047.
- 1066 Delanoë, J., and R. J. Hogan (2010), Combined CloudSat-CALIPSO-MODIS retrievals
1067 of the properties of ice clouds, *Journal of Geophysical Research: Atmospheres*, 115(4),
1068 D00H29, doi:10.1029/2009JD012346.
- 1069 Delanoë, J., A. Protat, J. Testud, D. Bouniol, A. J. Heymsfield, A. Bansemmer, P. R. A. Brown,
1070 and R. M. Forbes (2005), Statistical properties of the normalized ice particle size distribu-
1071 tion, *Journal of Geophysical Research*, 110(D10), D10,201, doi:10.1029/2004JD005405.
- 1072 Delanoë, J. M. E., and R. J. Hogan (2008), A variational scheme for retrieving ice cloud
1073 properties from combined radar, lidar, and infrared radiometer, *Journal of Geophysical
1074 Research*, 113(D7), D07,204, doi:10.1029/2007JD009000.
- 1075 Delanoë, J. M. E., A. J. Heymsfield, A. Protat, A. Bansemmer, and R. J. Hogan (2014), Nor-
1076 malized particle size distribution for remote sensing application, *Journal of Geophysical
1077 Research: Atmospheres*, 119(7), 4204–4227, doi:10.1002/2013JD020700.
- 1078 Erfani, E., and D. L. Mitchell (2017), Growth of ice particle mass and projected area during
1079 riming, *Atmospheric Chemistry and Physics*, 17(2), 1241–1257, doi:10.5194/acp-17-1241-
1080 2017.
- 1081 Field, P. R., and A. J. Heymsfield (2015), Importance of snow to global precipitation, *Geo-
1082 physical Research Letters*, 42(21), doi:10.1002/2015GL065497.
- 1083 Field, P. R., R. J. Hogan, P. R. A. Brown, A. J. Illingworth, T. W. Choullarton, and R. J. Cot-
1084 ton (2005), Parametrization of ice-particle size distributions for mid-latitude stratiform
1085 cloud, *Quarterly Journal of the Royal Meteorological Society*, 131(609), 1997–2017, doi:

- 1086 10.1256/qj.04.134.
- 1087 Field, P. R., A. J. Heymsfield, and A. Bansemer (2007), Snow Size Distribution Parame-
 1088 terization for Midlatitude and Tropical Ice Clouds, *Journal of the Atmospheric Sciences*,
 1089 *64*(12), 4346–4365, doi:10.1175/2007JAS2344.1.
- 1090 Francis, P. N., P. Hignett, and A. Macke (1998), The retrieval of cirrus cloud properties from
 1091 aircraft multi-spectral reflectance measurements during EUCREX'93, *Quarterly Journal*
 1092 *of the Royal Meteorological Society*, *124*(548), 1273–1291, doi:10.1002/qj.49712454812.
- 1093 Fujiyoshi, Y., and G. Wakahama (1985), On Snow Particles Comprising an Aggre-
 1094 gate, *Journal of the Atmospheric Sciences*, *42*(15), 1667–1674, doi:10.1175/1520-
 1095 0469(1985)042<1667:OSPCAA>2.0.CO;2.
- 1096 Grazioli, J., G. Lloyd, L. Panziera, C. R. Hoyle, P. J. Connolly, J. Henneberger, and A. Berne
 1097 (2015), Polarimetric radar and in situ observations of riming and snowfall microphysics
 1098 during CLACE 2014, *Atmospheric Chemistry and Physics*, *15*(23), 13,787–13,802, doi:
 1099 10.5194/acp-15-13787-2015.
- 1100 Grecu, M., W. S. Olson, S. J. Munchak, S. Ringerud, L. Liao, Z. Haddad, B. L. Kelley, and
 1101 S. F. McLaughlin (2016), The GPM Combined Algorithm, *Journal of Atmospheric and*
 1102 *Oceanic Technology*, *33*(10), 2225–2245, doi:10.1175/JTECH-D-16-0019.1.
- 1103 Harimaya, T., and M. Sato (1989), Measurement of the Riming Amount on Snowflakes,
 1104 *Journal of the Faculty of Science, Hokkaido University. Series 7, Geophysics*, *8*(4), 355–
 1105 366.
- 1106 Hawkness-Smith, L. (2010), A novel retrieval of liquid water path and a evaluation of the
 1107 representation of drizzle in numerical models, Ph.D. thesis, University of Reading.
- 1108 Haynes, J. M., T. S. L'Ecuyer, G. L. Stephens, S. D. Miller, C. Mitrescu, N. B. Wood, and
 1109 S. Tanelli (2009), Rainfall retrieval over the ocean with spaceborne W-band radar, *Journal*
 1110 *of Geophysical Research*, *114*, D00A22, doi:10.1029/2008JD009973.
- 1111 Helmus, J. J., and S. M. Collis (2016), The Python ARM Radar Toolkit (Py-ART), a Library
 1112 for Working with Weather Radar Data in the Python Programming Language, *Journal of*
 1113 *Open Research Software*, *4*(1), doi:10.5334/jors.119.
- 1114 Heymsfield, A. J. (1982), A Comparative Study of the Rates of Development of Potential
 1115 Graupel and Hail Embryos in High Plains Storms, *Journal of the Atmospheric Sciences*,
 1116 *39*(12), 2867–2897, doi:10.1175/1520-0469(1982)039<2867:ACSOTR>2.0.CO;2.
- 1117 Heymsfield, A. J., and M. Kajikawa (1987), An Improved Approach to Calculating Terminal
 1118 Velocities of Plate-like Crystals and Graupel, *Journal of the Atmospheric Sciences*, *44*(7),

- 1119 1088–1099, doi:10.1175/1520-0469(1987)044<1088:AIATCT>2.0.CO;2.
- 1120 Heymsfield, A. J., and L. M. Miloshevich (2003), Parameterizations for the
1121 Cross-Sectional Area and Extinction of Cirrus and Stratiform Ice Cloud Parti-
1122 cles, *Journal of the Atmospheric Sciences*, *60*(7), 936–956, doi:10.1175/1520-
1123 0469(2003)060<0936:PFTCSA>2.0.CO;2.
- 1124 Heymsfield, A. J., and C. D. Westbrook (2010), Advances in the Estimation of Ice Particle
1125 Fall Speeds Using Laboratory and Field Measurements, *Journal of the Atmospheric Sci-*
1126 *ences*, *67*(8), 2469–2482, doi:10.1175/2010JAS3379.1.
- 1127 Heymsfield, A. J., C. Schmitt, A. Bansemer, and C. H. Twohy (2010), Improved Representa-
1128 tion of Ice Particle Masses Based on Observations in Natural Clouds, *Journal of the Atmo-*
1129 *spheric Sciences*, *67*(10), 3303–3318, doi:10.1175/2010JAS3507.1.
- 1130 Heymsfield, A. J., S. Y. Matrosov, and N. B. Wood (2016), Toward Improving Ice Water
1131 Content and Snow-Rate Retrievals from Radars. Part I: X and W Bands, Emphasizing
1132 CloudSat, *Journal of Applied Meteorology and Climatology*, *55*(9), 2063–2090, doi:
1133 10.1175/JAMC-D-15-0290.1.
- 1134 Hiley, M. J., M. S. Kulie, and R. Bennartz (2011), Uncertainty Analysis for CloudSat Snow-
1135 fall Retrievals, *Journal of Applied Meteorology and Climatology*, *50*(2), 399–418, doi:
1136 10.1175/2010JAMC2505.1.
- 1137 Hogan, R. J. (2007), A Variational Scheme for Retrieving Rainfall Rate and Hail Reflectiv-
1138 ity Fraction from Polarization Radar, *Journal of Applied Meteorology and Climatology*,
1139 *46*(10), 1544–1564, doi:10.1175/JAM2550.1.
- 1140 Hogan, R. J. (2008), Fast Lidar and Radar Multiple-Scattering Models. Part I: Small-Angle
1141 Scattering Using the Photon Variance–Covariance Method, *Journal of the Atmospheric*
1142 *Sciences*, *65*(12), 3621–3635, doi:10.1175/2008JAS2642.1.
- 1143 Hogan, R. J. (2014), Fast Reverse-Mode Automatic Differentiation using Expression
1144 Templates in C++, *ACM Transactions on Mathematical Software*, *40*(4), 1–16, doi:
1145 10.1145/2560359.
- 1146 Hogan, R. J. (2017), Adept 2.0: a combined automatic differentiation and array library for
1147 C++, doi:10.5281/ZENODO.1004730.
- 1148 Hogan, R. J., and A. J. Illingworth (1999), The Potential of Spaceborne Dual-
1149 Wavelength Radar to Make Global Measurements of Cirrus Clouds, *Journal*
1150 *of Atmospheric and Oceanic Technology*, *16*(5), 518–531, doi:10.1175/1520-
1151 0426(1999)016<0518:TPOSDW>2.0.CO;2.

- 1152 Hogan, R. J., and C. D. Westbrook (2014), Equation for the Microwave Backscatter Cross
1153 Section of Aggregate Snowflakes Using the Self-Similar Rayleigh-Gans Approximation,
1154 *Journal of the Atmospheric Sciences*, 71(9), 3292–3301, doi:10.1175/JAS-D-13-0347.1.
- 1155 Hogan, R. J., P. N. Francis, H. Flentje, A. J. Illingworth, M. Quante, and J. Pelon (2003),
1156 Characteristics of mixed-phase clouds. I: Lidar, radar and aircraft observations from
1157 CLARE'98, *Quarterly Journal of the Royal Meteorological Society*, 129(592), 2089–2116,
1158 doi:10.1256/rj.01.208.
- 1159 Hogan, R. J., M. D. Behera, E. J. O'Connor, and A. J. Illingworth (2004), Estimate of the
1160 global distribution of stratiform supercooled liquid water clouds using the LITE lidar,
1161 *Geophysical Research Letters*, 31(5), L05,106, doi:10.1029/2003GL018977.
- 1162 Hogan, R. J., L. Tian, P. R. A. Brown, C. D. Westbrook, A. J. Heymsfield, and J. D. Eastment
1163 (2012), Radar Scattering from Ice Aggregates Using the Horizontally Aligned Oblate
1164 Spheroid Approximation, *Journal of Applied Meteorology and Climatology*, 51(3), 655–
1165 671, doi:10.1175/JAMC-D-11-074.1.
- 1166 Hogan, R. J., R. Honeyager, J. Tyynelä, and S. Kneifel (2017), Calculating the millimetre-
1167 wave scattering phase function of snowflakes using the self-similar Rayleigh-Gans Ap-
1168 proximation, *Quarterly Journal of the Royal Meteorological Society*, 143(703), 834–844,
1169 doi:10.1002/qj.2968.
- 1170 Hou, A. Y., R. K. Kakar, S. Neeck, A. A. Azarbarzin, C. D. Kummerow, M. Kojima, R. Oki,
1171 K. Nakamura, and T. Iguchi (2014), The Global Precipitation Measurement Mission, *Bul-
1172 letin of the American Meteorological Society*, 95(5), 701–722, doi:10.1175/BAMS-D-13-
1173 00164.1.
- 1174 Illingworth, A. J., and T. M. Blackman (2002), The Need to Represent Raindrop Size Spec-
1175 tra as Normalized Gamma Distributions for the Interpretation of Polarization Radar
1176 Observations, *Journal of Applied Meteorology*, 41(3), 286–297, doi:10.1175/1520-
1177 0450(2002)041<0286:TNTRRS>2.0.CO;2.
- 1178 Illingworth, A. J., R. J. Hogan, E. J. O'Connor, D. Bouniol, J. Delanoë, J. Pelon, A. Pro-
1179 tat, M. E. Brooks, N. Gaussiat, D. R. Wilson, D. P. Donovan, H. K. Baltink, G.-J. van
1180 Zadelhoff, J. D. Eastment, J. W. F. Goddard, C. L. Wrench, M. Haeffelin, O. A. Krasnov,
1181 H. W. J. Russchenberg, J.-M. Piriou, F. Vinit, A. Seifert, A. M. Tompkins, and U. Willén
1182 (2007), Cloudnet, *Bulletin of the American Meteorological Society*, 88(6), 883–898, doi:
1183 10.1175/BAMS-88-6-883.

- 1184 Illingworth, A. J., H. W. Barker, A. Beljaars, M. Ceccaldi, H. Chepfer, N. Clerbaux,
1185 J. Cole, J. Delanoë, C. Domenech, D. P. Donovan, S. Fukuda, M. Hiraakata, R. J. Hogan,
1186 A. Huenerbein, P. Kollias, T. Kubota, T. Nakajima, T. Y. Nakajima, T. Nishizawa, Y. Ohno,
1187 H. Okamoto, R. Oki, K. Sato, M. Satoh, M. W. Shephard, A. Velázquez-Blázquez,
1188 U. Wandinger, T. Wehr, and G.-J. van Zadelhoff (2015), The EarthCARE Satellite: The
1189 Next Step Forward in Global Measurements of Clouds, Aerosols, Precipitation, and
1190 Radiation, *Bulletin of the American Meteorological Society*, *96*(8), 1311–1332, doi:
1191 10.1175/BAMS-D-12-00227.1.
- 1192 Jiang, Z., M. Oue, J. Verlinde, E. E. Clothiaux, K. Aydin, G. Botta, and Y. Lu (2017), What
1193 Can We Conclude about the Real Aspect Ratios of Ice Particle Aggregates from Two-
1194 Dimensional Images?, *Journal of Applied Meteorology and Climatology*, *56*(3), 725–734,
1195 doi:10.1175/JAMC-D-16-0248.1.
- 1196 Jullien, R. (1992), The application of fractals to colloidal aggregation, *Croatica Chemica*
1197 *Acta*, *65*(2), 215–235.
- 1198 Kalesse, H., W. Szyrmer, S. Kneifel, P. Kollias, and E. Luke (2016), Fingerprints of a riming
1199 event on cloud radar Doppler spectra: observations and modeling, *Atmospheric Chemistry*
1200 *and Physics*, *16*(5), 2997–3012, doi:10.5194/acp-16-2997-2016.
- 1201 Khvorostyanov, V. I., and J. A. Curry (2005), Fall Velocities of Hydrometeors in the Atmo-
1202 sphere: Refinements to a Continuous Analytical Power Law, *Journal of the Atmospheric*
1203 *Sciences*, *62*(12), 4343–4357, doi:10.1175/JAS3622.1.
- 1204 Kneifel, S., U. Löhnert, A. Battaglia, S. Crewell, and D. Siebler (2010), Snow scattering sig-
1205 nals in ground-based passive microwave radiometer measurements, *Journal of Geophys-
1206 ical Research*, *115*(D16), D16,214, doi:10.1029/2010JD013856.
- 1207 Kneifel, S., M. Maahn, G. Peters, and C. Simmer (2011), Observation of snowfall with a
1208 low-power FM-CW K-band radar (Micro Rain Radar), *Meteorology and Atmospheric*
1209 *Physics*, *113*(1-2), 75–87, doi:10.1007/s00703-011-0142-z.
- 1210 Kneifel, S., A. von Lerber, J. Tiira, D. Moisseev, P. Kollias, and J. Leinonen (2015), Ob-
1211 served relations between snowfall microphysics and triple-frequency radar measure-
1212 ments, *Journal of Geophysical Research: Atmospheres*, *120*(12), 6034–6055, doi:
1213 10.1002/2015JD023156.
- 1214 Kneifel, S., J. Dias Neto, D. Ori, D. Moisseev, J. Tyynelä, I. S. Adams, K.-S. Kuo, R. Ben-
1215 nartz, A. Berne, E. E. Clothiaux, P. Eriksson, A. J. Geer, R. Honeyager, J. Leinonen, and
1216 C. D. Westbrook (2018), Summer Snowfall Workshop: Scattering Properties of Realis-

- 1217 tic Frozen Hydrometeors from Simulations and Observations, as well as Defining a New
1218 Standard for Scattering Databases, *Bulletin of the American Meteorological Society*, 99(3),
1219 ES55–ES58, doi:10.1175/BAMS-D-17-0208.1.
- 1220 Kollias, P., S. Tanelli, A. Battaglia, and A. Tatarevic (2014), Evaluation of EarthCARE
1221 Cloud Profiling Radar Doppler Velocity Measurements in Particle Sedimentation
1222 Regimes, *Journal of Atmospheric and Oceanic Technology*, 31(2), 366–386, doi:
1223 10.1175/JTECH-D-11-00202.1.
- 1224 Kulie, M. S., and R. Bennartz (2009), Utilizing Spaceborne Radars to Retrieve Dry
1225 Snowfall, *Journal of Applied Meteorology and Climatology*, 48(12), 2564–2580, doi:
1226 10.1175/2009JAMC2193.1.
- 1227 Kulie, M. S., L. Milani, N. B. Wood, S. A. Tushaus, R. Bennartz, and T. S. L’Ecuyer (2016),
1228 A Shallow Cumuliform Snowfall Census Using Spaceborne Radar, *Journal of Hydromete-*
1229 *orology*, 17(4), 1261–1279, doi:10.1175/JHM-D-15-0123.1.
- 1230 Langleben, M. P. (1954), The terminal velocity of snowflakes, *Quarterly Journal of the*
1231 *Royal Meteorological Society*, 80(344), 174–181, doi:10.1002/qj.49708034404.
- 1232 Leinonen, J., and D. Moisseev (2015), What do triple-frequency radar signatures reveal
1233 about aggregate snowflakes?, *Journal of Geophysical Research: Atmospheres*, 120(1),
1234 229–239, doi:10.1002/2014JD022072.
- 1235 Leinonen, J., and W. Szyrmer (2015), Radar signatures of snowflake riming: A modeling
1236 study, *Earth and Space Science*, 2(8), 346–358, doi:10.1002/2015EA000102.
- 1237 Leinonen, J., M. D. Lebsock, G. L. Stephens, and K. Suzuki (2016), Improved Retrieval of
1238 Cloud Liquid Water from CloudSat and MODIS, *Journal of Applied Meteorology and*
1239 *Climatology*, 55(8), 1831–1844, doi:10.1175/JAMC-D-16-0077.1.
- 1240 Li, H., D. Moisseev, and A. von Lerber (2018), How Does Riming Affect Dual-Polarization
1241 Radar Observations and Snowflake Shape?, *Journal of Geophysical Research: Atmo-*
1242 *spheres*, 123(11), 6070–6081, doi:10.1029/2017JD028186.
- 1243 Liebe, H. J. (1985), An updated model for millimeter wave propagation in moist air, *Radio*
1244 *Science*, 20(5), 1069–1089.
- 1245 Lin, Y., and B. A. Colle (2011), A New Bulk Microphysical Scheme That Includes Rim-
1246 ing Intensity and Temperature-Dependent Ice Characteristics, *Monthly Weather Review*,
1247 139(3), 1013–1035, doi:10.1175/2010MWR3293.1.
- 1248 Lin, Y., L. J. Donner, and B. A. Colle (2011), Parameterization of Riming Intensity and Its
1249 Impact on Ice Fall Speed Using ARM Data, *Monthly Weather Review*, 139(3), 1036–1047,

- 1250 doi:10.1175/2010MWR3299.1.
- 1251 Liu, G. (2008), Deriving snow cloud characteristics from CloudSat observations, *Journal of*
1252 *Geophysical Research*, 113(D8), D00A09, doi:10.1029/2007JD009766.
- 1253 Löhnert, U., S. Kneifel, A. Battaglia, M. Hagen, L. Hirsch, and S. Crewell (2011), A Mul-
1254 tisensor Approach Toward a Better Understanding of Snowfall Microphysics: The
1255 TOSCA Project, *Bulletin of the American Meteorological Society*, 92(5), 613–628, doi:
1256 10.1175/2010BAMS2909.1.
- 1257 Maahn, M., and U. Löhnert (2017), Potential of Higher-Order Moments and Slopes of the
1258 Radar Doppler Spectrum for Retrieving Microphysical and Kinematic Properties of Arc-
1259 tic Ice Clouds, *Journal of Applied Meteorology and Climatology*, 56(2), 263–282, doi:
1260 10.1175/JAMC-D-16-0020.1.
- 1261 Maahn, M., U. Löhnert, P. Kollias, R. C. Jackson, and G. M. McFarquhar (2015), Developing
1262 and Evaluating Ice Cloud Parameterizations for Forward Modeling of Radar Moments
1263 Using in situ Aircraft Observations, *Journal of Atmospheric and Oceanic Technology*,
1264 32(5), 880–903, doi:10.1175/JTECH-D-14-00112.1.
- 1265 Mace, G., and S. Benson (2017), Diagnosing Cloud Microphysical Process Information from
1266 Remote Sensing Measurements—A Feasibility Study Using Aircraft Data. Part I: Tropical
1267 Anvils Measured during TC4, *Journal of Applied Meteorology and Climatology*, 56(3),
1268 633–649, doi:10.1175/JAMC-D-16-0083.1.
- 1269 Mason, S. L., J. C. Chiu, R. J. Hogan, and L. Tian (2017), Improved rain-rate and drop-
1270 size retrievals from airborne and spaceborne Doppler radar, *Atmospheric Chemistry and*
1271 *Physics Discussions*, pp. 1–34, doi:10.5194/acp-2017-280.
- 1272 Mitchell, D. (1996), Use of mass-and area-dimensional power laws for determining precipita-
1273 tion particle terminal velocities, *Journal of the atmospheric sciences*.
- 1274 Mitchell, D. L., and A. J. Heymsfield (2005), Refinements in the Treatment of Ice Particle
1275 Terminal Velocities, Highlighting Aggregates, *Journal of the Atmospheric Sciences*, 62(5),
1276 1637–1644, doi:10.1175/JAS3413.1.
- 1277 Mitchell, D. L., R. Zhang, and R. L. Pitter (1990), Mass-Dimensional Relationships for Ice
1278 Particles and the Influence of Riming on Snowfall Rates, *Journal of Applied Meteorology*,
1279 29(2), 153–163, doi:10.1175/1520-0450(1990)029<0153:MDRFIP>2.0.CO;2.
- 1280 Moisseev, D., A. von Lerber, and J. Tiira (2017), Quantifying the effect of riming on snow-
1281 fall using ground-based observations, *Journal of Geophysical Research: Atmospheres*,
1282 122, doi:10.1002/2016JD026272.

- 1283 Morrison, H., and J. A. Milbrandt (2015), Parameterization of Cloud Microphysics Based
1284 on the Prediction of Bulk Ice Particle Properties. Part I: Scheme Description and Ideal-
1285 ized Tests, *Journal of the Atmospheric Sciences*, 72(1), 287–311, doi:10.1175/JAS-D-14-
1286 0065.1.
- 1287 Morrison, H., J. A. Milbrandt, G. H. Bryan, K. Ikeda, S. A. Tessendorf, and G. Thompson
1288 (2015), Parameterization of Cloud Microphysics Based on the Prediction of Bulk Ice Par-
1289 ticle Properties. Part II: Case Study Comparisons with Observations and Other Schemes,
1290 *Journal of the Atmospheric Sciences*, 72(1), 312–339, doi:10.1175/JAS-D-14-0066.1.
- 1291 Mosimann, L. (1995), An improved method for determining the degree of snow crystal rim-
1292 ing by vertical Doppler radar, *Atmospheric Research*, 37(4), 305–323, doi:10.1016/0169-
1293 8095(94)00050-N.
- 1294 National Academies of Sciences Engineering and Medicine (2018), *Thriving on Our Chang-*
1295 *ing Planet: A Decadal Strategy for Earth Observation from Space*, National Academies
1296 Press, Washington, D.C., doi:10.17226/24938.
- 1297 Newman, A. J., P. A. Kucera, and L. F. Bliven (2009), Presenting the Snowflake Video
1298 Imager (SVI), *Journal of Atmospheric and Oceanic Technology*, 26(2), 167–179, doi:
1299 10.1175/2008JTECHA1148.1.
- 1300 Palerme, C., J. E. Kay, C. Genthon, T. L’Ecuyer, N. B. Wood, and C. Claud (2014), How
1301 much snow falls on the Antarctic ice sheet?, *The Cryosphere*, 8(4), 1577–1587, doi:
1302 10.5194/tc-8-1577-2014.
- 1303 Petäjä, T., E. J. O’Connor, D. Moisseev, V. A. Sinclair, A. J. Manninen, R. Väänänen, A. von
1304 Lerber, J. A. Thornton, K. Nicoll, W. Petersen, V. Chandrasekar, J. N. Smith, P. M. Win-
1305 kler, O. Krüger, H. Hakola, H. Timonen, D. Brus, T. Laurila, E. Asmi, M.-L. Riekkola,
1306 L. Mona, P. Massoli, R. Engelmann, M. Komppula, J. Wang, C. Kuang, J. Bäck, A. Virta-
1307 nen, J. Levula, M. Ritsche, and N. Hickmon (2016), BA ECC: A Field Campaign to Elu-
1308 cidate the Impact of Biogenic Aerosols on Clouds and Climate, *Bulletin of the American*
1309 *Meteorological Society*, 97(10), 1909–1928, doi:10.1175/BAMS-D-14-00199.1.
- 1310 Rodgers, C. D. (2000), *Inverse methods for atmospheric sounding: theory and practice*,
1311 World Scientific, Singapore.
- 1312 Schmitt, C. G., and A. J. Heymsfield (2010), The Dimensional Characteristics of Ice Crystal
1313 Aggregates from Fractal Geometry, *Journal of the Atmospheric Sciences*, 67(5), 1605–
1314 1616, doi:10.1175/2009JAS3187.1.

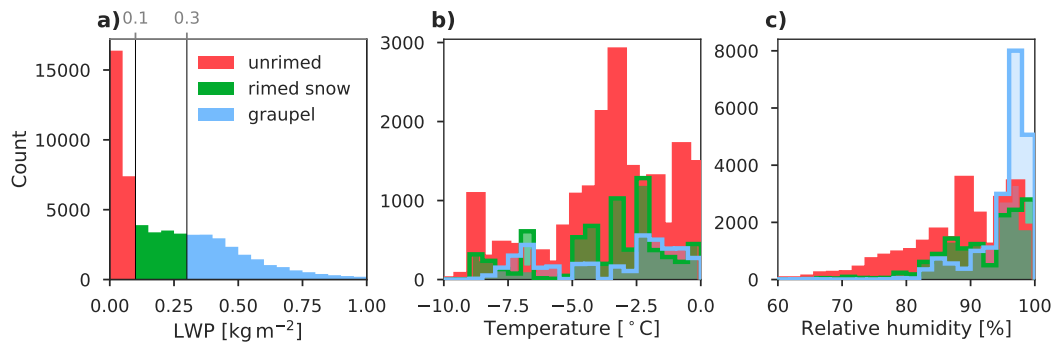
- 1315 Shupe, M. D., P. Kollias, S. Y. Matrosov, and T. L. Schneider (2004), Deriving Mixed-Phase
 1316 Cloud Properties from Doppler Radar Spectra, *Journal of Atmospheric and Oceanic Tech-*
 1317 *nology*, 21(4), 660–670, doi:10.1175/1520-0426(2004)021<0660:DMCPFD>2.0.CO;2.
- 1318 Stein, T. H. M., C. D. Westbrook, and J. C. Nicol (2015), Fractal geometry of aggregate
 1319 snowflakes revealed by triple-wavelength radar measurements, *Geophysical Research Let-*
 1320 *ters*, 42(1), 176–183, doi:10.1002/2014GL062170.
- 1321 Stephens, G. L., D. G. Vane, R. J. Boain, G. G. Mace, K. Sassen, Z. Wang, A. J. Illingworth,
 1322 E. J. O’Connor, W. B. Rossow, S. L. Durden, and others (2002), The CloudSat mission
 1323 and the A-Train: A new dimension of space-based observations of clouds and precipita-
 1324 tion, *Bulletin of the American Meteorological Society*, 83(12), 1771–1790.
- 1325 Szyrmer, W., and I. Zawadzki (2014), Snow Studies. Part III: Theoretical Derivations for
 1326 the Ensemble Retrieval of Snow Microphysics from Dual-Wavelength Vertically Pointing
 1327 Radars, *Journal of the Atmospheric Sciences*, 71(3), 1158–1170, doi:10.1175/JAS-D-12-
 1328 0285.1.
- 1329 Tan, I., T. Storelvmo, and M. D. M. Zelinka (2016), Observational constraints on mixed-
 1330 phase clouds imply higher climate sensitivity, *Science*, 352(6282), 224–227, doi:
 1331 10.1126/science.aad5300.
- 1332 Tanelli, S., S. L. Durden, E. Im, G. M. Heymsfield, P. Racette, and D. O. Starr (2009), Next-
 1333 generation spaceborne Cloud Profiling Radars, in *2009 IEEE Radar Conference*, pp. 1–4,
 1334 IEEE, doi:10.1109/RADAR.2009.4977116.
- 1335 Testud, J., S. Oury, R. A. Black, P. Amayenc, and X. Dou (2001), The Concept of a Normalized
 1336 Distribution to Describe Raindrop Spectra: A Tool for Cloud Physics
 1337 and Cloud Remote Sensing, *Journal of Applied Meteorology*, 40(6), 1118–1140, doi:
 1338 10.1175/1520-0450(2001)040<1118:TCOND>2.0.CO;2.
- 1339 Tiira, J., D. N. Moisseev, A. von Lerber, D. Ori, A. Tokay, L. F. Bliven, and W. Petersen
 1340 (2016), Ensemble mean density and its connection to other microphysical properties of
 1341 falling snow as observed in Southern Finland, *Atmospheric Measurement Techniques*,
 1342 9(9), 4825–4841, doi:10.5194/amt-9-4825-2016.
- 1343 Twomey, S. (1977), Introduction to the Mathematics of Inversion in Remote Sensing and
 1344 Indirect, *Elsevier Scientific Publishing*.
- 1345 von Lerber, A., D. Moisseev, L. F. Bliven, W. Petersen, A.-M. Harri, and V. Chandrasekar
 1346 (2017), Microphysical Properties of Snow and Their Link to Ze-S Relations during
 1347 BAecc 2014, *Journal of Applied Meteorology and Climatology*, 56(6), 1561–1582, doi:

1348 10.1175/JAMC-D-16-0379.1.

1349 Westbrook, C. D., R. C. Ball, P. R. Field, and A. J. Heymsfield (2004), Theory of growth by
1350 differential sedimentation, with application to snowflake formation, *Physical Review E*,
1351 *70*(2), 021,403, doi:10.1103/PhysRevE.70.021403.

1352 Yin, M., G. Liu, R. Honeyager, and F. Joseph Turk (2017), Observed differences of
1353 triple-frequency radar signatures between snowflakes in stratiform and convective
1354 clouds, *Journal of Quantitative Spectroscopy and Radiative Transfer*, *193*, 13–20, doi:
1355 10.1016/J.JQSRT.2017.02.017.

1356 Zikmunda, J., and G. Vali (1972), Fall Patterns and Fall Velocities of Rimed Ice Crys-
1357 tals, *Journal of the Atmospheric Sciences*, *29*(7), 1334–1347, doi:10.1175/1520-
1358 0469(1972)029<1334:FPAFVO>2.0.CO;2.



859 **Figure 12.** Histograms of remote-sensed LWP (a) and surface temperature (b) and relative humidity (c)
 860 data from all snow events from SNEX IOP, grouped into three LWP classes.

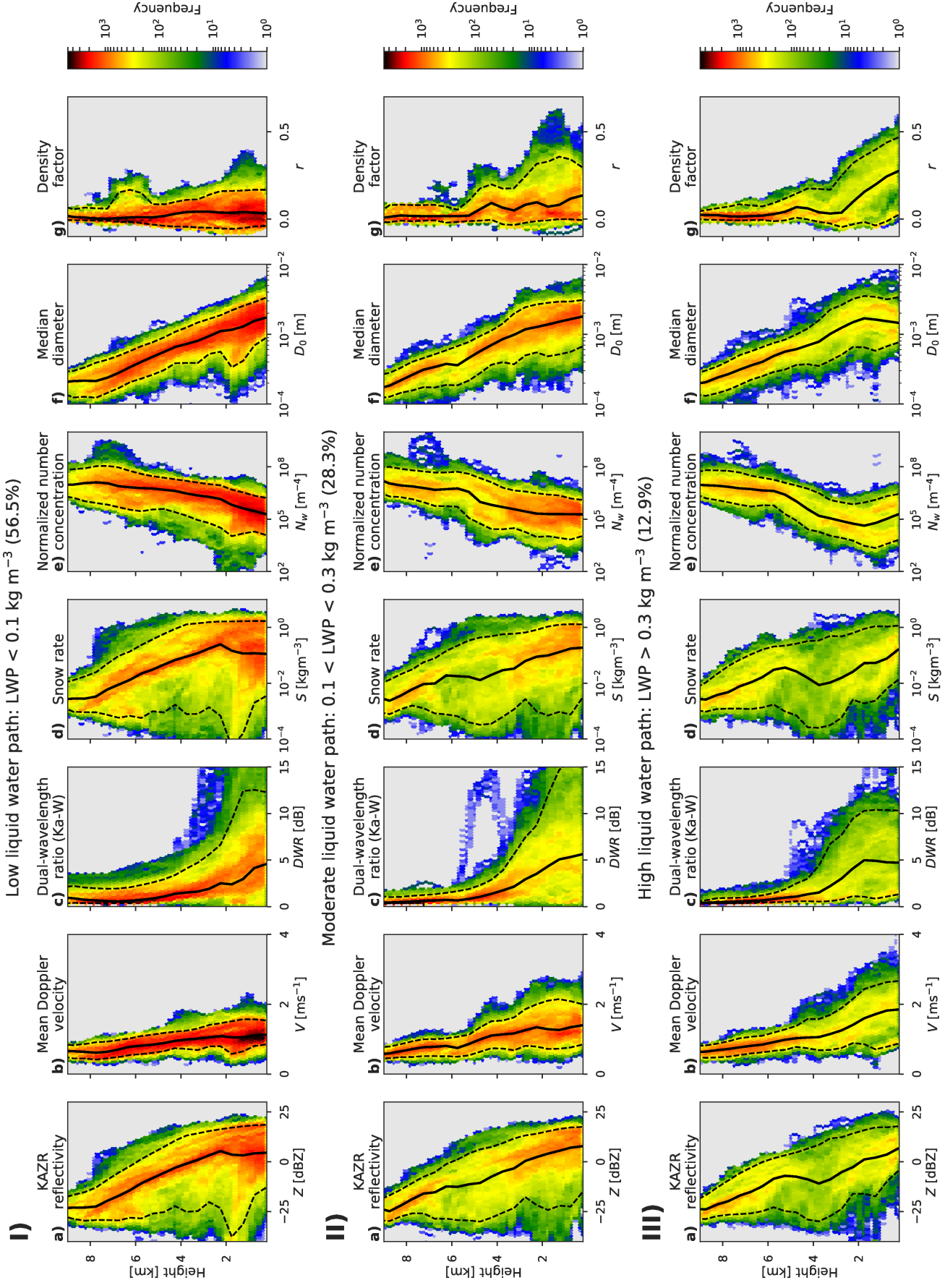


Figure 13. Joint histograms for $ZZY-\alpha_v N'_0 r'$ CAPTIVATE retrieval of forward-modelled (a-c) and retrieved (d-g) variables against altitude for snow events during the SNEX 2014 IOP. Snow events are divided into three regimes, unrimed snow (I) and graupel (II), using LWP as a proxy for riming. Solid black lines indicate the median—and dashed lines the 5th and 95th percentiles—of the forward modelled or retrieved values at each height.